GeoStorage

Vol. 2, No. 1, p. 40-60, 2026

Research article

# A Physics-Informed Neural Network Approach for Constitutive Modeling of Oil-Well Cement Slurries Under Cyclic Loading

Hanzhi Yang[1,2,3], Yue Yang[1,2,3], Wei Guo[1,2,3*], Lei Wang[2,4], Zhenhui Bi[4], Guokai Zhao[4], Jian Zhao[5]

[1] *State Key Laboratory of Deep Earth Exploration and Imaging, College of Construction Engineering, Jilin University, Changchun 130026, China*
[2] *Key Lab of Geo-Exploration Instrumentation, Ministry of Education, Jilin University, Changchun 130026, China*
[3] *Engineering Research Center of Geothermal Resources Development Technology and Equipment, Ministry of Education, Jilin University, Changchun 130026, China*
[4] *State Key Laboratory of Geomechanics and Geotechnical Engineering Safety, Institute of Rock and Soil Mechanics, Chinese Academy of Sciences, Wuhan 430071, China*
[5] *Department of Civil and Environmental Engineering, University of Alberta, Edmonton, T6G 1H9, Canada*

**Keywords:**
Oil-well cement
hysteresis loop evolution
cyclic constitutive modeling
physics-informed neural networks (PINN)
cyclic loading path

**Cited as:**
Yang HZ, Yang Y, Guo W, et al. 2026. A Physics-Informed Neural Network Approach for Constitutive Modeling of Oil-Well Cement Slurries Under Cyclic Loading. *GeoStorage*, 2(1), 40-60.
https://doi.org/10.46690/gs.2026.01.04

**Abstract:**
Deep learning (DL) based on Artificial Neural Networks (ANN) demonstrates robust performance, strong nonlinear mapping capabilities, and powerful self-learning capacities, enabling its widespread application in learning and predicting stress-strain constitutive relationships under quasi-static loading paths (e.g., uniaxial/triaxial compression tests). However, significant gaps remain in applying ANN methods to learn, characterize, or predict constitutive relationships for geotechnical materials under complex multi-cycle dynamic loading paths. This limitation primarily arises from the nonlinearity, variability, and complexity inherent in cyclic stress-strain hysteresis loops. This study systematically investigates oil-well cement sheaths subjected to high-intensity multi-frequency cyclic compression. Samples were set and cured at four downhole temperatures (25, 90, 115, and 140 °C), then tested under four constant-amplitude loading levels (30%, 50%, 70%, and 90%). A comprehensive analysis of 480 hysteresis loops from 16 sample groups was conducted, evaluating accumulated plastic strain, dissipation energy proportion, and the proportion of plastic damage energy. The analysis reveals that conventional fatigue life prediction models fail to effectively capture the complex evolutionary characteristics of hysteresis loops. Subsequently, the cyclic stress-strain constitutive relationship was treated as time-series data. Through preprocessing and cycle-by-cycle segmentation of mechanical test data, single-step rolling prediction of hysteresis loops was achieved. An LSTM (The Long Short-Term Memory) architecture was developed to address long-term dependencies and complex nonlinear features in different hysteresis loops. By constructing a Physics-Informed Neural Network (PINN) that integrates physical laws and data patterns, the physics-guided learning capability of the improved model was enhanced. Recursive prediction with additional physical constraints enabled full-process continuous rolling prediction, demonstrating superior predictive performance. The proposed methodology provides novel perspectives for advancing intelligent inversion methods in geotechnical engineering applications under dynamic loading conditions.

## 1 Introduction

In subsurface oil and gas engineering, hardened oil-well cement is commonly used as cement sheath with an annular structure between the casing and the formation, serving as the primary barrier to maintaining wellbore integrity. This cement sheath performs multiple critical functions, including sealing

Yandy Scientific Press

* Corresponding author.
*E-mail address*: yanghanzhi@jlu.edu.cn (Yang HZ); yangyue@jlu.edu.cn (Yang Y); guowei6981@jlu.edu.cn (Guo W); lwang@whrsm.ac.cn (Wang L); bzh199511998@163.com (Bi ZH); gkzhao@whrsm.ac.cn (Zhao GK); jian19@ualberta.ca (Zhao J)

Received Dec. 20, 2025; revised Jan. 6, 2026; accepted Jan. 16, 2026; available online Feb. 6, 2026.

**Tab. 1** Summary of methods for learning and predicting constitutive relationships of geotechnical materials based on artificial neural network (ANN)

| Application | Specific Algorithms | Descriptions | References |
|---|---|---|---|
| Quasi-static loading | Radial basis function neural network (RBFNN) | The Gaussian function is used as the activation function. | (Tan and Wang, 2001; Peng et al., 2008) |
| | Multi-Layer Perceptron (MLP) | The information flows forward from the input nodes to the output nodes. | (Nardin et al., 2003; Banimahd et al., 2005; Rafiai and Jafari, 2011) |
| | Fully-connected neural network (FCNN) | All the nodes in one layer are connected to the neurons in the next layer. | (Gorji et al., 2020) |
| | Convolutional neural networks (CNN) | It can learn based on the shared-weight architecture of the convolution kernels or filters. | (Wu et al., 2023; Yang et al., 2020) |
| | Feedback neural network (FBN) | Feedback connections from output layer to input layer. | (Penumadu and Zhao, 1999; Habibagahi and Bamdad, 2003) |
| | Recurrent neural network (RNN) | Feedback connections from a hidden and output layer to input layer. | (Zhu et al., 1998; Romo et al., 2001) |
| | Long short-term memory (LSTM) | A gating mechanism utilizing three gates (input, output, and forget gates). | (Shi et al., 2022; Li et al., 2023) |
| | Genetic algorithm-based neural network | The genetic algorithm (GA) is applied. | (Chen et al., 2004; Johari et al., 2011) |
| Dynamic loading | Back propagation neural network (BPNN) | The back propagation (BP) algorithm is applied. | (Ghaboussi and Sidarta, 1998; Youssef et al., 2006; Rashidian and Hassanlourad, 2014) |
| | Time-delay neural network (TDNN) | It can classify patterns with shift-invariance and model context at each layer of the network. | (Basheer, 2002) |
| | Temporal Convolutional Network (TCN) | Comprises dilated causal 1D convolutional layers that maintain identical input and output lengths. | (Wang et al., 2022) |
| | Gated recurrent unit (GRU) | A gating mechanism utilizing two gates (reset and update gates). | (Qiu et al., 2021; Zhang et al., 2021; Xiong et al., 2023) |

the annular space between the casing and the formation, preventing fluid migration across different strata by providing zonal isolation, and protecting the casing from excessive formation pressures during drilling and production operations (Karakosta et al., 2015; Pang et al., 2021). Consequently, maintaining excellent mechanical properties of the cement sheath over its entire service life is crucial.

During oil and gas productions, the cement sheath is frequently subjected to high-magnitude, high-frequency cyclic compressive loads. For example, such cyclic loads arise in deep shale gas development scenarios involving staged hydraulic fracturing with high-pressure slurry injection (Gholami et al., 2016). Similarly, cyclic injection-withdrawal operations in depleted gas reservoir storage facilities and salt cavern gas storage facilities also fall under the category of cyclic loads. These cyclic loads can induce progressive, irreversible damage in the cement sheath in the form of brittle microcracking and plastic deformation, while the casing and surrounding formation typically exhibit predominantly elastic recovery during the unloading phase (Eilers et al., 1983; Grabowski and Gillott, 1989). This mismatch in mechanical deformation leads to gradual debonding at the cement interfaces, resulting in the formation of micro-annuli. Such interfacial degradation can cause sustained casing pressure (SCP) or hydrocarbon leakage, both of which pose serious risks to well integrity, production, and operational safety (Diaz et al., 2020). According to case statistics compiled by the British Geological Survey (BGS) on storage incidents in gas reservoirs over the past century, the United States has experienced 14 accidents involving depleted oil and gas reservoirs, with wellbore seal failures during injection–withdrawal operations accounting for approximately 31% of total incidents due to gas leakage (Evans, 2007; Yin et al., 2024).

Similar to other brittle materials such as concrete and rock, the fatigue damage and ultimate failure of hardened cement paste is governed by the initiation and propagation of microcracks (Beaudoin and Feldman, 1985). To further investigate the fatigue performance of oil-well cement under downhole cyclic loading conditions have been systematically investigated by uniaxial and triaxial cyclic loading experiments (Shadravan et al., 2015; Deng et al., 2020; Yang et al., 2024a) and theoretical modelling. For instance, Li et al. and Xi et al. successively compared the fatigue performance of conventional cement slurries and latex-modified cement slurries in triaxial cyclic loading tests, and they have consistently observed that oil-well cement experiences significant cumulative plastic strain when subjected to high-frequency and high-magnitude cyclic loads

**Tab. 2** HTHP compressive cyclic loading testing plans on oil-well cement slurries considering different loading levels

| Testing number | Curing condition | | Testing condition | | | |
|---|---|---|---|---|---|---|
| | Curing temperature (°C) | Curing pressure (MPa) | Testing temperature (°C) | Confining pressure (MPa) | Number of cycles | Loading level |
| 1 | 25 | 20 | 25 | 20 | 30 | 30% |
| 2 | 25 | 20 | 25 | 20 | 30 | 50% |
| 3 | 25 | 20 | 25 | 20 | 30 | 70% |
| 4 | 25 | 20 | 25 | 20 | 30 | 90% |
| 5 | 90 | 20 | 90 | 20 | 30 | 30% |
| 6 | 90 | 20 | 90 | 20 | 30 | 50% |
| 7 | 90 | 20 | 90 | 20 | 30 | 70% |
| 8 | 90 | 20 | 90 | 20 | 30 | 90% |
| 9 | 115 | 20 | 115 | 20 | 30 | 30% |
| 10 | 115 | 20 | 115 | 20 | 30 | 50% |
| 11 | 115 | 20 | 115 | 20 | 30 | 70% |
| 12 | 115 | 20 | 115 | 20 | 30 | 90% |
| 13 | 140 | 20 | 140 | 20 | 30 | 30% |
| 14 | 140 | 20 | 140 | 20 | 30 | 50% |
| 15 | 140 | 20 | 140 | 20 | 30 | 70% |
| 16 | 140 | 20 | 140 | 20 | 30 | 90% |

(Li et al., 2007; Xi et al., 2020). Theoretically, current studies on the fatigue behavior of brittle materials, including cement, rock, and concrete, under cyclic loading primarily focus on reverse S-shaped fatigue life prediction models (Xiao et al., 2009). These models typically establish the relationship between a damage variable and fatigue life (in terms of loading cycles) based on continuum damage mechanics (CDM) or micromechanical damage theories. Common approaches include the residual strain method, maximum strain method, dissipated energy method, acoustic emission cumulative count method, and ultrasonic wave velocity method (Xiao et al., 2010).

The cyclic constitutive model of oil-well cement can be constructed by integrating experimental data with theoretical methods. However, prior experimental research has largely remained at the phenomenological level. The fatigue performance of oil-well cements, especially under varying mix designs and downhole temperature–pressure conditions, often requires extensive and repetitive experimental validation. Theoretically, while significant efforts have been made in studying cyclic constitutive models, existing fatigue life prediction models often fail to capture the dynamic stress–strain constitutive behavior under cyclic loading.

Intelligent inversion methods, including artificial neural networks (ANNs), are particularly well-suited for capturing the complex nonlinear mapping between stress and strain in geotechnical materials. Various well-established ANN models have been successfully applied to the learning and prediction of stress–strain relationships under quasi-static uniaxial and triaxial loading conditions (Gorji et al., 2020; Shi et al., 2022; Wu et al., 2023; Li et al., 2023), as illustrated in Table 1. Furthermore, the adoption of Physics-informed Neural Networks (PINN), a deep learning approach capable of unifying data and physical principles, could further enhance the generalization capability, applicability, and predictive performance of deep learning models (Carleo et al., 2019; Karniadakis et al., 2021; Wang et al., 2023).

However, a comprehensive review of the literature reveals that current ANN-based approaches to constitutive modeling are primarily limited to quasi-static loading scenarios (Gorji et al., 2020; Shi et al., 2022; Wu et al., 2023; Li et al., 2023). ANN models for describing or predicting the stress–strain behavior of geotechnical materials under cyclic loading and unloading conditions remain underdeveloped. Existing studies are generally limited to relatively simple cases involving only a small number of loading cycles, typically no more than three. For instance, Ellis and co-workers were the first to apply a backpropagation neural network (BPNN) to effectively learn the constitutive stress–strain relationships of soils subjected to undrained triaxial compression with varying stress histories, including one cycle of unloading and reloading (Ellis et al., 1995). Subsequently, in the studies conducted by Basheer (2000, 2002), both BPNN and time-delay neural network (TDNN) models were used to simulate soil behavior under stress paths involving single and double unloading–reloading cycles, ultimately producing high-accuracy predictions of real soil responses (Basheer, 2000, 2002). All of the above models adopt a direct learning strategy in which the entire stress–strain curve is input into the ANN in a single stage. A major limitation of this approach is that, when applied to cyclic loading scenarios, the complexity of the stress–strain curve increases

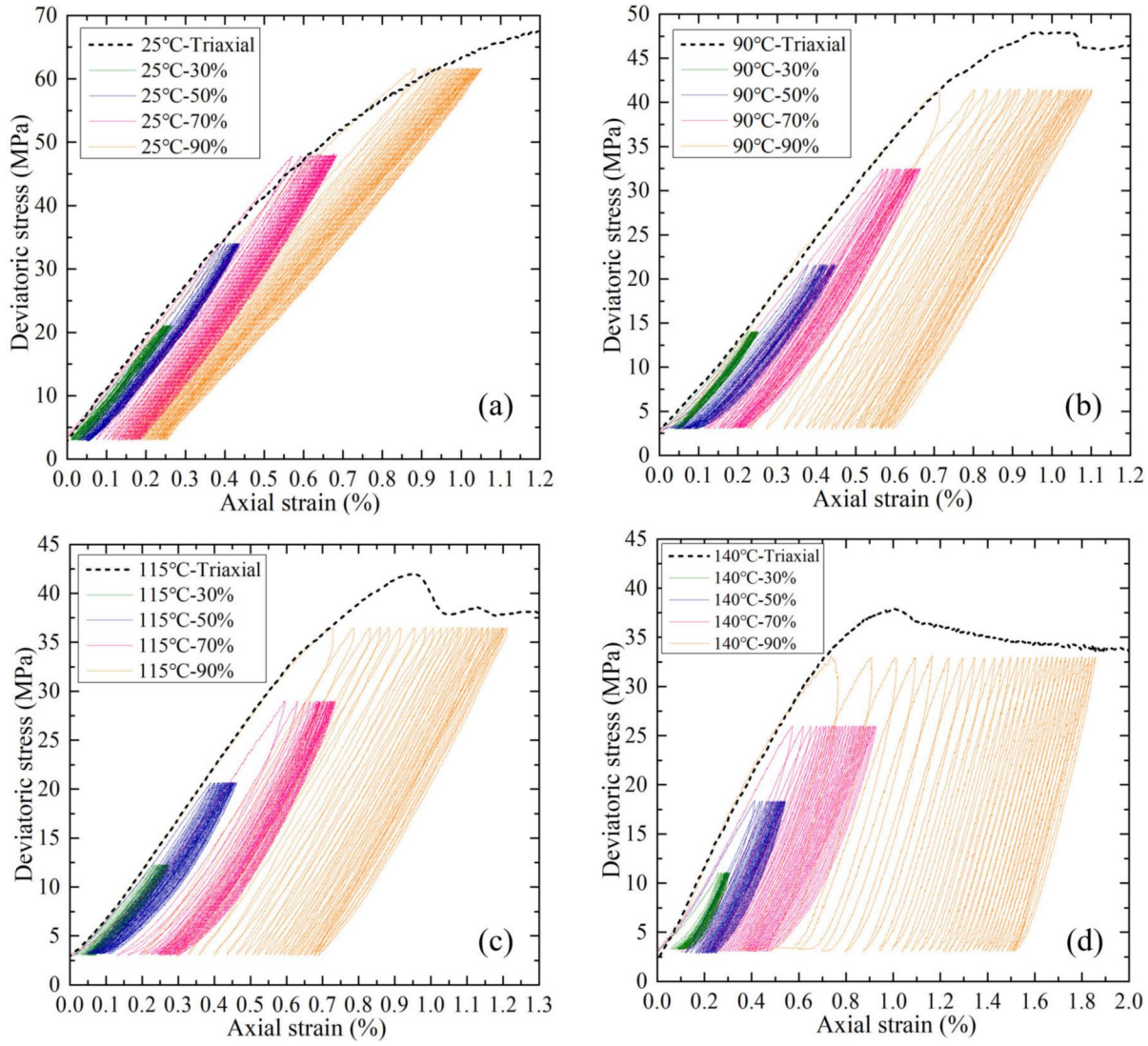


**Fig. 1** Compressive cyclic stress–strain curves of oil-well cement slurries considering different loading levels. Samples at downhole temperatures of (a) 25 °C, (b) 90 °C, (c) 115 °C, and (d) 140 °C

significantly, making it considerably more difficult to achieve accurate learning outcomes.

In this study, based on the energy balance theory in rock mechanics, the fatigue characteristics of 480 hysteresis loops (derived from 16 sets of oil-well cement samples) – including the accumulated plastic strain, proportion of dissipated energy, and proportion of plastic damage energy – were analyzed. The results demonstrated that conventional fatigue life prediction models are inadequate for capturing the complex evolutionary characteristics of the hysteresis behavior, thereby underscoring the necessity of directly constructing constitutive models for cyclic stress and strain responses. Subsequently, by applying normalization, down-sampling, and cycle-by-cycle segmentation to the experimental data obtained under cyclic loading conditions, we introduced, for the first time, a deep learning framework guided by physics-informed mechanisms to the study of constitutive relationships between cyclic stress and strain. The methodology and findings presented in this paper collectively form a novel framework for cyclic constitutive modeling, effectively overcoming the limitations of existing mechanical constitutive models characterized by complex formulations and limited applicability.

## 2 Methodology

### 2.1 Description of experimental data

A series of cyclic loading experiments were systematically conducted on oil-well cement samples cured under four downhole temperature conditions: 25 °C, 90 °C, 115 °C, and 140 °C. During testing, a confining pressure of 20 MPa was applied. Four loading levels were selected, corresponding to 30 %, 50 %, 70 %, and 90 % of the peak load, in order to evaluate the fatigue performance of the cement. The lower limit of the cyclic load was set at 1.5 kN. The number of loading cycles was fixed at 30, which is consistent with the maximum number of fracturing stages typically encountered during multi-stage hydraulic fracturing in shale gas wells (Gholami et al., 2016). The experiments were performed under axial force control, with both loading and unloading rates set at 0.5 kN per second.

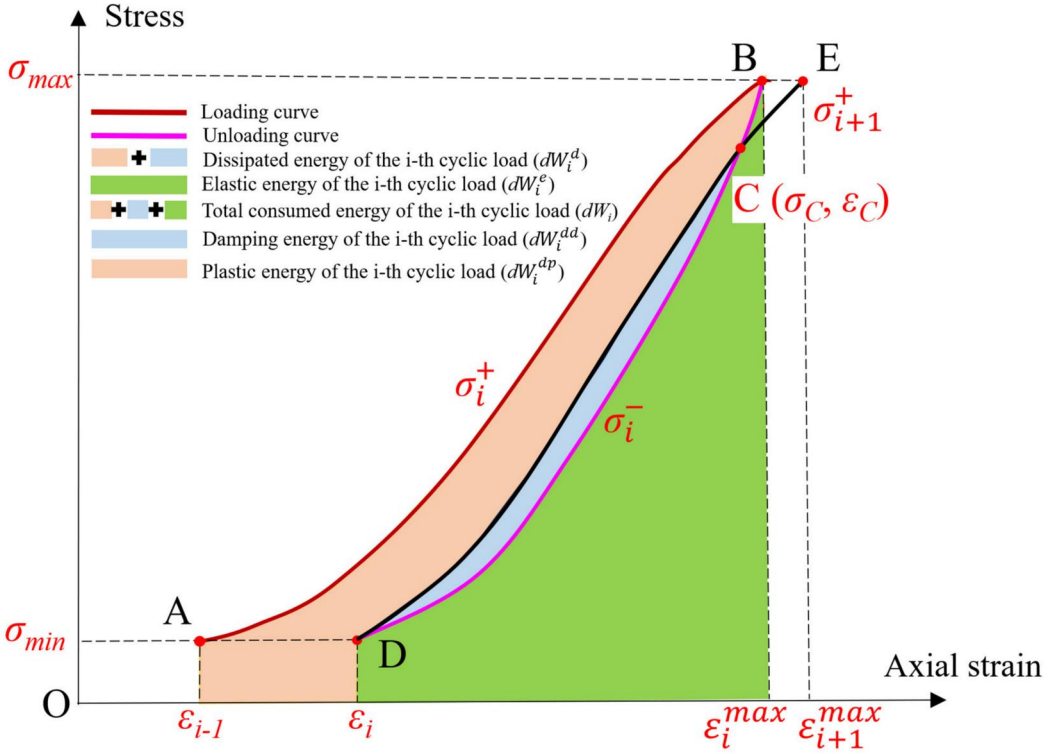


**Fig. 2** Schematic of the cyclic stress-strain curve in the *i*-th cycle

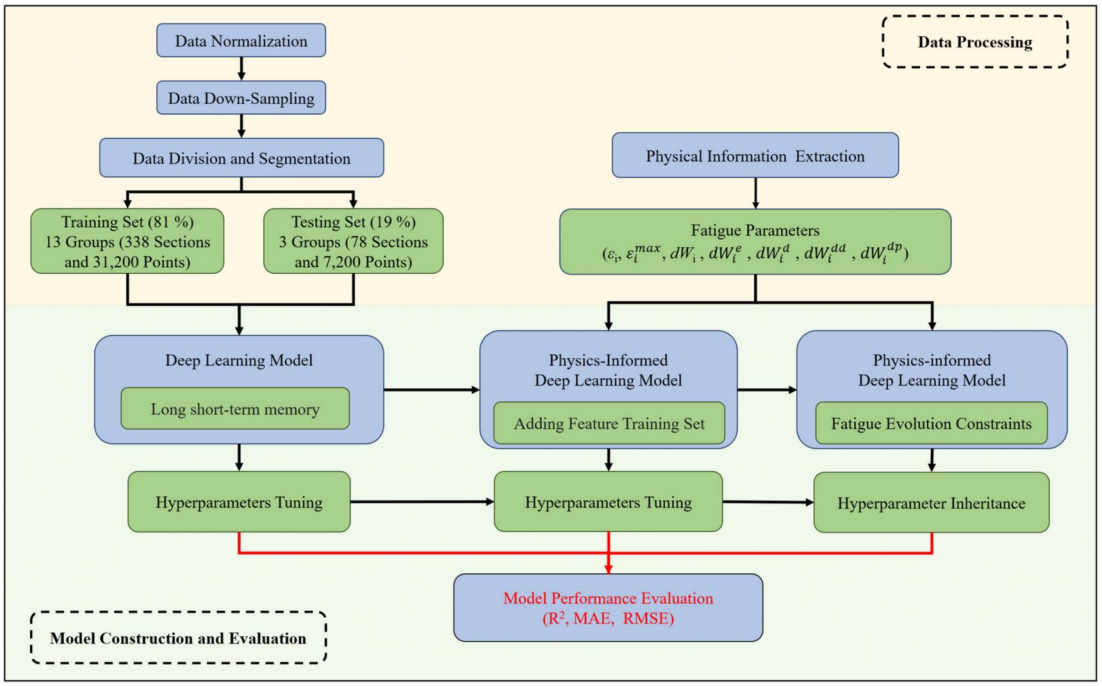


**Fig. 3** Workflow for describing and predicting cyclic stress-strain constitutive relationships based on deep learning architecture

Details of the experimental scheme are provided in Table 2, and the original data curves are illustrated in Fig. 1.

Previous studies have demonstrated that the stress and strain curves under cyclic loading exhibit nonlinear characteristics during both the loading and unloading phases (Shadravan et al., 2015; Deng et al., 2020; Yang et al., 2024b). As the stress increases during the loading phase, the oil-well cement undergoes greater plastic deformation, and the stress and strain curve progressively develops an upward-convex shape. During the unloading phase, as the applied stress decreases, the compressed pores within the cement begin to rebound, resulting in a gradual

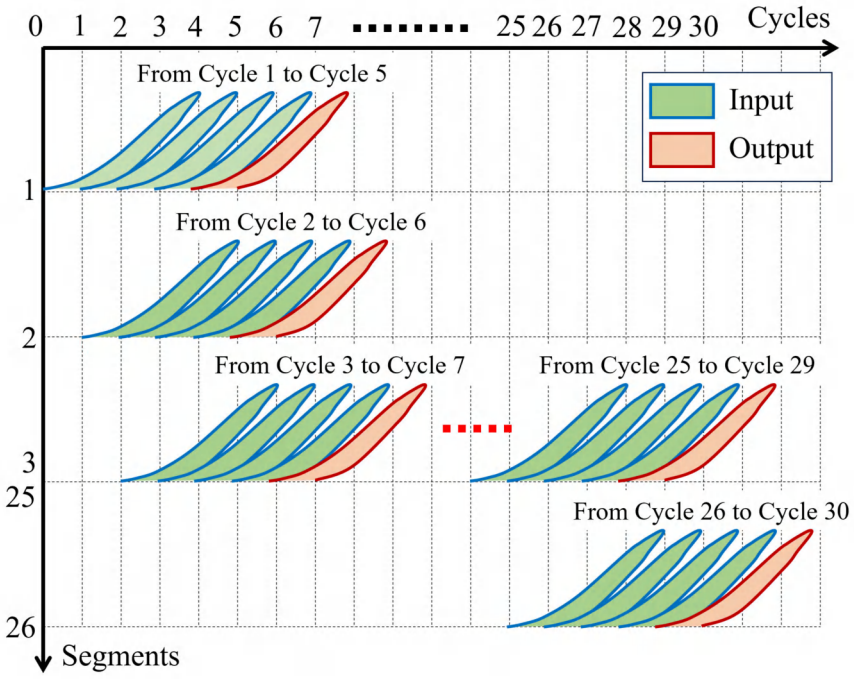


**Fig. 4** Schematic of cycle-by-cycle data segmentation and model input-output configuration

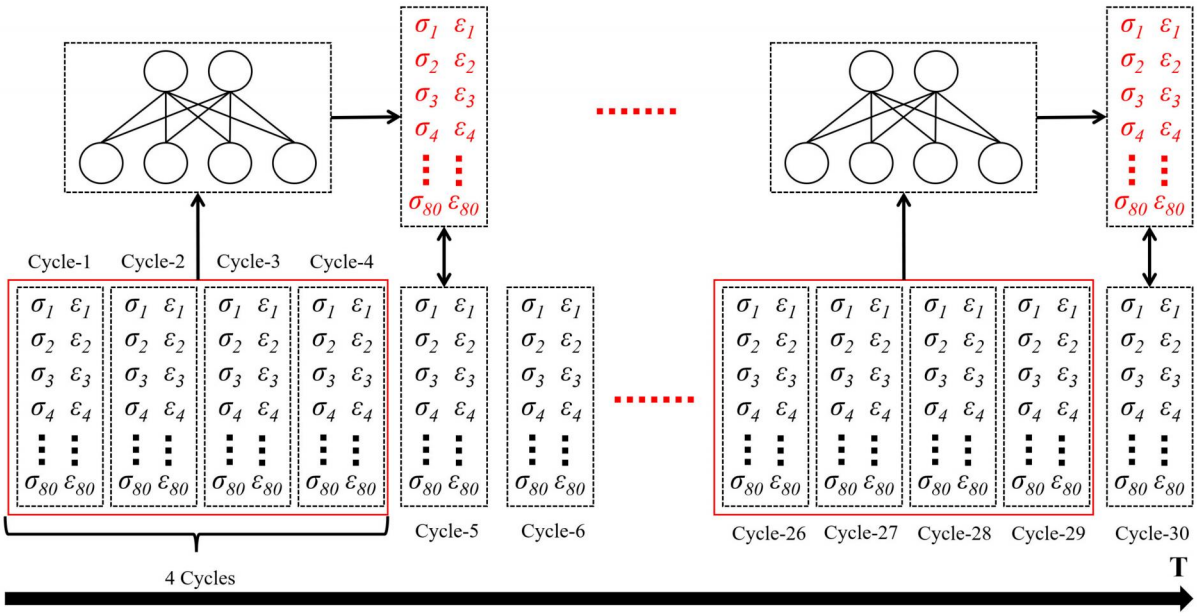


**Fig. 5** The schematic diagram of the single-step training and prediction process for LSTM model

reduction of the elastic modulus. Consequently, the stress and strain curve during unloading tends to exhibit a downward-convex shape. Together, these loading and unloading responses form the complete cyclic hysteresis loop.

## 2.2 Complex evolution characteristics of cyclic hysteresis loops

The mechanical response of oil-well cement under cyclic loading is critical for evaluating its resistance to fatigue damage in downhole environments. The shape of the hysteresis loop reflects the constitutive behavior between stress and strain during cyclic loading and unloading, as well as the evolution of mechanical parameters such as elastic modulus and energy dissipation (Mayergoyz, 1985). Among these, the energy dissipated during each cycle characterizes the material's capacity to resist internal damage and plastic deformation induced by external loading (Song et al., 2018). As shown in Fig. 2, a typical stress and strain curve for the $i$-th cycle includes a loading path from point A to point B, followed by an unloading path from point B through point C to point D. Points A and D correspond to the residual plastic strains after the $(i-1)$-th and $i$-th cycles, denoted as $\varepsilon_{i-1}$ and $\varepsilon_i$, respectively. These strains share the

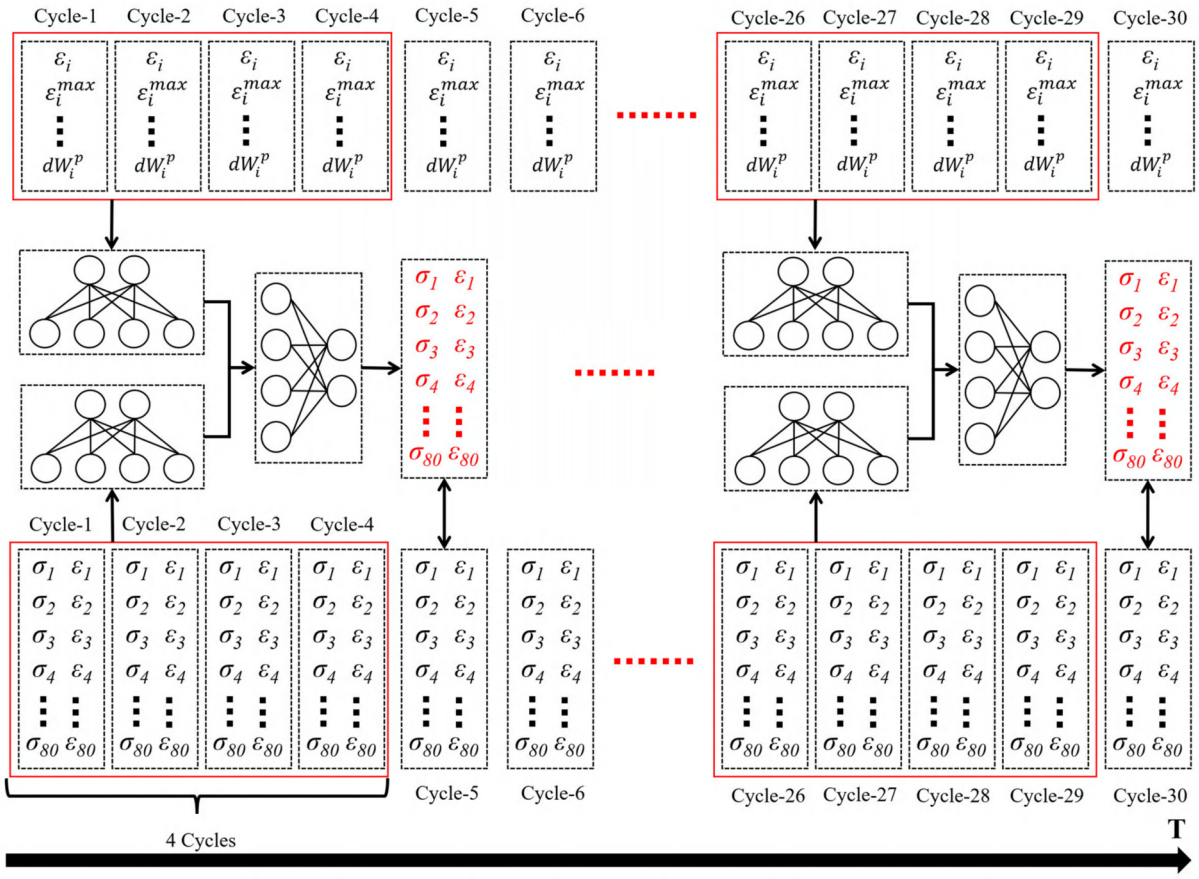


**Fig. 6** The schematic diagram of the single-step training and prediction process for PINN models

same stress value $\sigma_{\min}$, which represents the lower bound of the cyclic load. The stress at point B, denoted as $\sigma_{\max}$, represents the upper bound of the cyclic load, and the corresponding strain is the maximum strain in the $i$-th cycle,. Using definite integral methods (Meng et al., 2016), the total input energy $dW_i$, the recoverable elastic energy , and the dissipated energy for the $i$-th cycle can be calculated as follows:

$$dW_i^e = \int_{\varepsilon_i}^{\varepsilon_i^{\max}} \overline{\sigma}_i \, d\varepsilon \tag{1}$$

$$dW_i = \int_{\varepsilon_{i-1}}^{\varepsilon_i^{\max}} \sigma_i^+ \, d\varepsilon \tag{2}$$

$$dW_i^d = dW_i - dW_i^e = \int_{\varepsilon_{i-1}}^{\varepsilon_i^{\max}} \sigma_i^+ \, d\varepsilon - \int_{\varepsilon_i}^{\varepsilon_i^{\max}} \overline{\sigma}_i \, d\varepsilon \tag{3}$$

$$\eta_i = \frac{dW_i^d}{dW_i} = 1 - \frac{dW_i^e}{dW_i} \tag{4}$$

The dissipated energy proportion, denoted as $\eta_i$, is defined as the ratio between the dissipated energy and the total input energy in the $i$-th cycle. An increase in $\eta_i$ indicates that the cement material has accumulated more plastic strain or internal damage. The energy dissipated during the loading process is primarily consumed by mechanisms associated with internal damage evolution and plastic deformation within the cement matrix.

To further investigate the evolution patterns of the hysteresis loop shape, the dissipated energy contained within the loop can be subdivided based on the theory of viscoelastic deformation. Wu and Li et al. have both pointed out that, during the unloading phase, if the dissipation of energy due to heat exchange, thermal radiation, and acoustic emission is neglected, nonlinear hysteretic behavior can still occur in the stress and strain response (Wu et al., 2020; Li et al., 2021a). This is primarily caused by interfacial friction between material particles and the viscosity of pore fluids, resulting in a characteristic hysteresis loop that is wider in the middle and narrower at both ends. As shown in Fig.2, the total dissipated energy within a hysteresis loop consists of two components. The first is the plastic damage energy, denoted as $dW_i^{dp}$, which is associated with residual plastic strain, plastic deformation, and microcrack development. The second is the damping energy, denoted as $dW_i^{dd}$, which represents the energy dissipated by the material in overcoming viscous resistance. Notably, the unloading curve of the $i$-th cycle and the loading curve of the $(i + 1)$-th cycle intersect precisely at point C. The path from point C to point D during unloading and the return from point D to point C during reloading represent a viscoelastic deformation process. In this process, no elastic energy is lost, and the energy dissipation is entirely attributed to the work done by damping forces. The

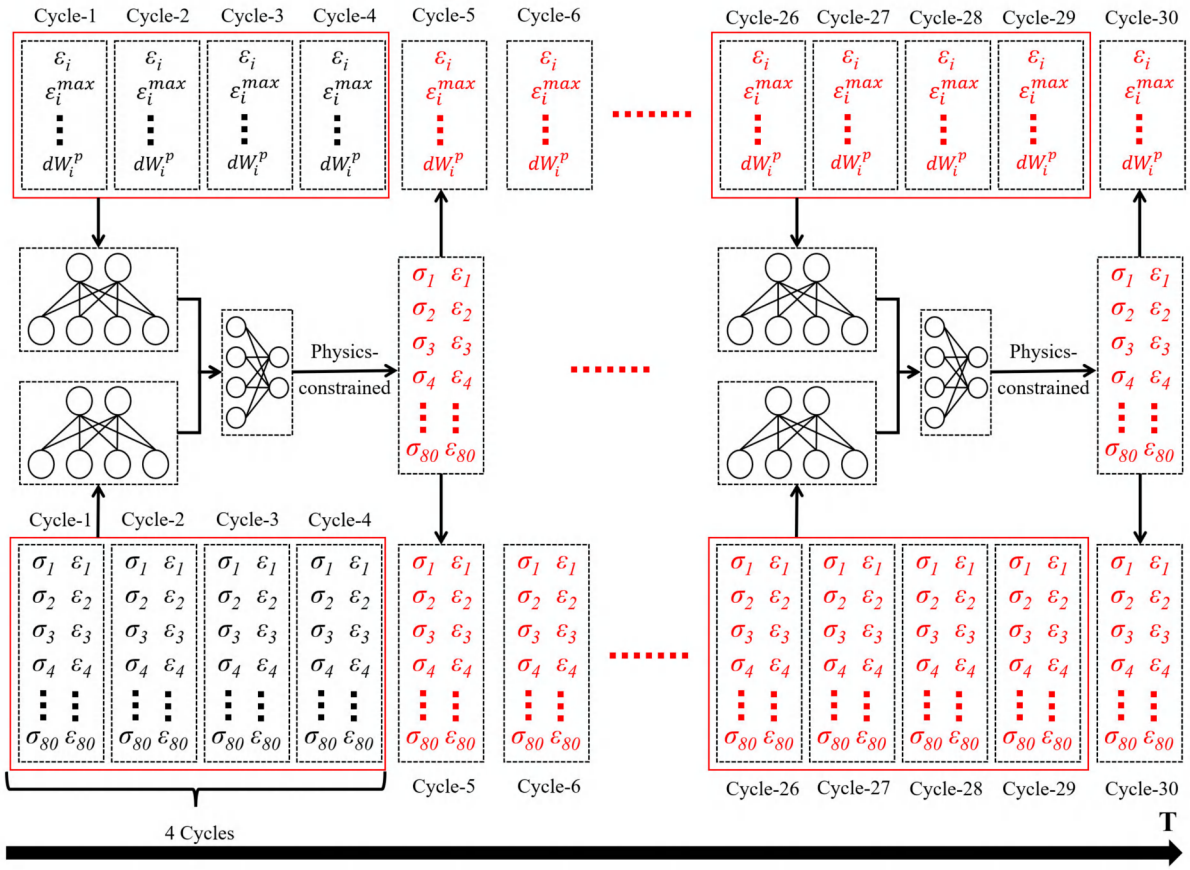


**Fig. 7** The schematic diagram of the full-cycle prediction process for PINN model

corresponding formulas for calculating the damping energy and plastic damage energy are given as follows:

$$dW_i^{dd} = \int_{\varepsilon_i}^{\varepsilon_C} (\sigma_{i+1}^{+} - \sigma_i^{-}) d\varepsilon \tag{5}$$

$$dW_i^{dp} = dW_i^{d} - dW_i^{dd} = \int_{\varepsilon_{i-1}}^{\varepsilon_i^{\max}} \sigma_i^{+} d\varepsilon - \int_{\varepsilon_i}^{\varepsilon_i^{\max}} \sigma_i^{-} d\varepsilon - \int_{\varepsilon_i}^{\varepsilon_C} (\sigma_{i+1}^{+} - \sigma_i^{-}) d\varepsilon \tag{6}$$

Furthermore, the proportion of plastic damage energy, denoted as $\xi$, can be calculated for each sample to quantify the fraction of the total dissipated energy within each hysteresis loop that is attributed to plastic deformation and microcrack-induced damage. This proportion is defined as the ratio of the plastic damage energy $dW_i^{dp}$ to the total dissipated energy in the $i$-th cycle. The corresponding calculation formula is given as follows:

$$\zeta_i = \frac{dW_i^{\mathrm{dp}}}{dW_i^{\mathrm{d}}} = 1 - \frac{dW_i^{\mathrm{dd}}}{dW_i^{\mathrm{d}}} \tag{7}$$

## 2.3 Development for the physics-informed neural network

For oil-well cement with the same mix design, the hardened cement prepared under different curing temperatures exhibits significantly different material properties. As a result, it becomes increasingly difficult to accurately describe the stress and strain constitutive behavior of high-temperature cement under cyclic loading and unloading using traditional continuum mechanics theories, including elastoplastic mechanics and damage mechanics. Compared with traditional constitutive models of geomaterials based on explicit mathematical equations, ANN models can effectively approximate stress–strain experimental curves with complex nonlinear functional relationships. Their main advantages include the ability to directly train on experimental data using inputs and outputs (supervised learning) without any assumptions about the relationship between the variables, as well as the capacity to learn and train on large datasets, which further enhances the model's prediction accuracy and applicability as more data are incorporated.

In this study, by employing a deep learning model based on time-series analysis and further segmenting the cyclic stress and strain curves according to individual loading cycles, the cyclic constitutive behavior could be treated as time-series data. This approach enables investigation into the evolving characteristics of cyclic responses, particularly the hysteresis loops, over successive loading cycles. The LSTM algorithm was selected to capture the long-term evolutionary patterns and nonlinear characteristics inherent in hysteresis loops. Additionally, the physics-informed constraint method was employed to progres-

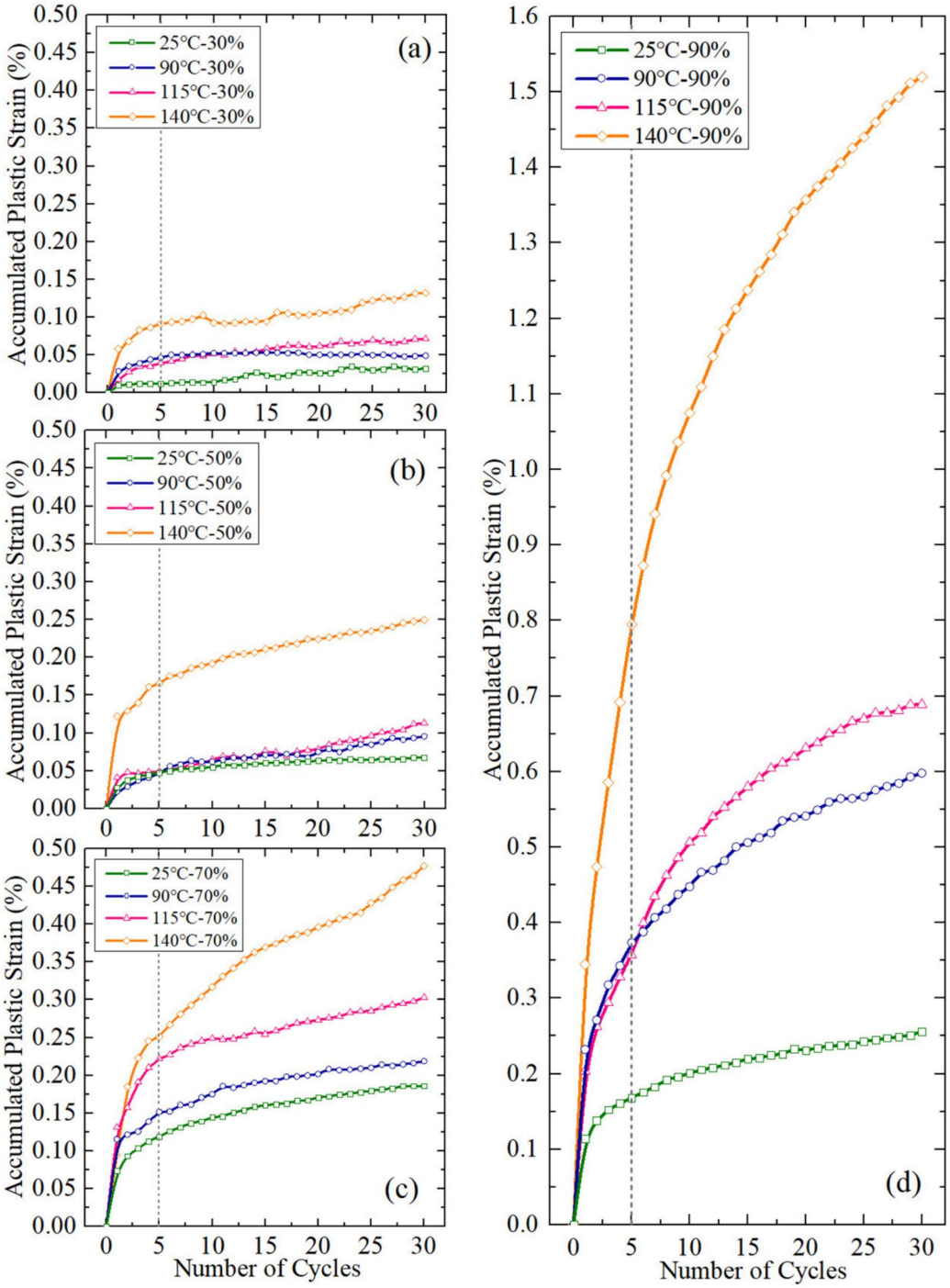


**Fig. 8** Accumulated plastic strain of oil-well cement slurries in cyclic stress–strain curves considering different loading levels and downhole temperatures. Samples at downhole temperatures of (a)25 °C, (b)90 °C, (c)115 °C, and (d)140 °C

sively enhance both single-step and full-cycle prediction accuracy of the cyclic curves. The overall research framework is outlined in Fig. 3.

### 2.3.1 Data preprocessing

This process includes data normalization and the unification of sequence length across all input samples. Normalizing the input data helps accelerate model training and mitigates issues related to gradient explosion or vanishing gradients. Experimental data stored in Excel format are read using the Pandas library, and then scaled to the range of [0, 1] using the MinMaxScaler preprocessing function from the Scikit-learn library. In addition, to ensure consistent sequence length (i.e., number of time steps) across all samples, integer factor-based downsampling is applied. In this study, each cycle is standardized to include 40 loading points and 40 unloading points.

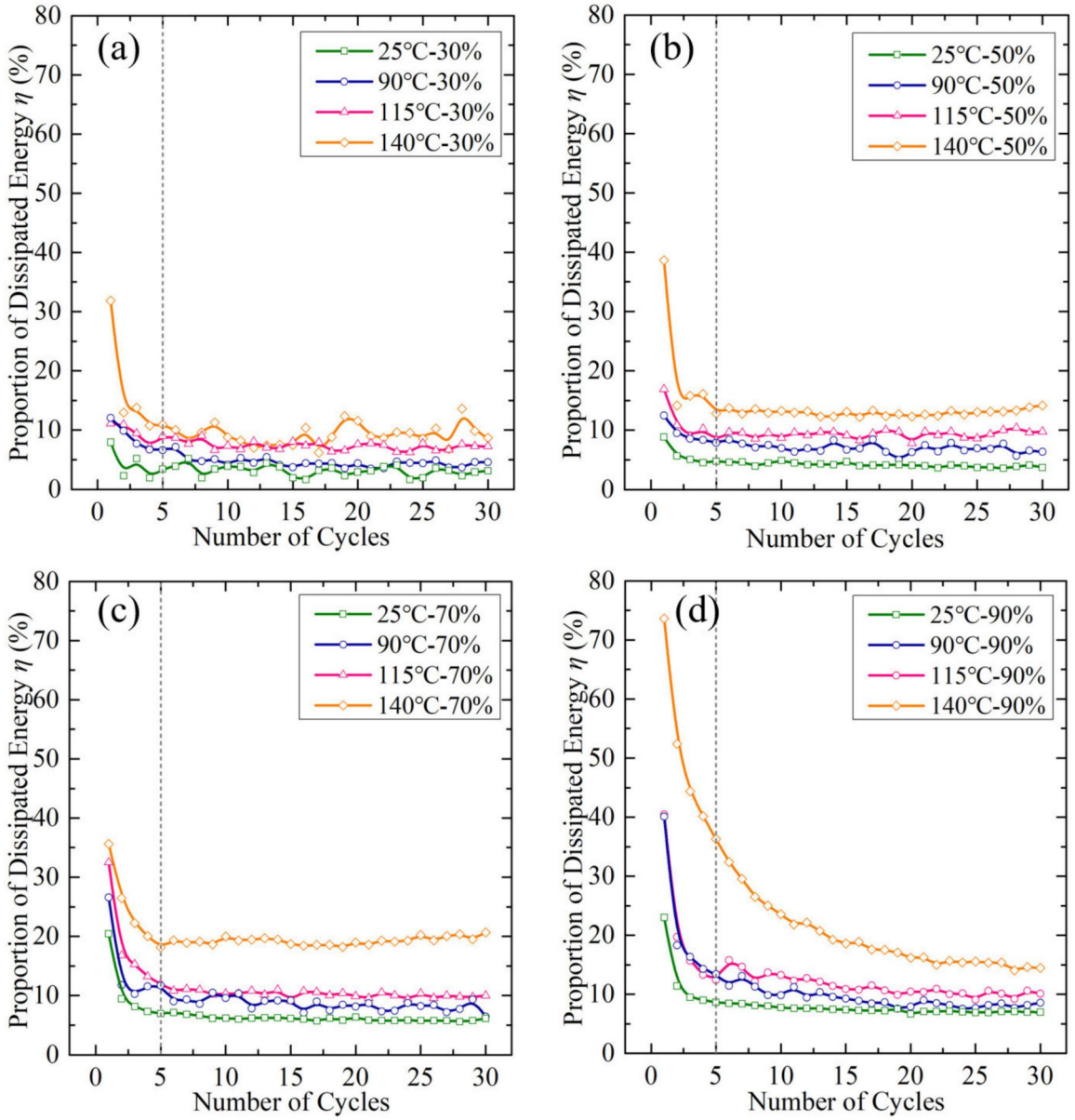


**Fig. 9** Dissipated energy proportion of oil-well cement slurries in cyclic stress–strain curves considering different loading levels and downhole temperatures. Samples at loading levels of (a)30 %, (b)50 %, (c)70 %, and (d)90 %

### 2.3.2 Data division and cycle-by-cycle segmentation

The process also includes the division of the dataset into a training set and a prediction set, as well as the further segmentation of data by loading cycles. In the training and prediction set split, the goal is to ensure that the deep learning model maintains strong generalization capability, allowing it to adapt effectively to previously unseen data while preserving high prediction accuracy. To this end, the cyclic loading curves of 3 randomly selected specimens, accounting for 19 % of the dataset, are designated as the prediction set, while the remaining 13 specimens, representing 81 %, form the training set. Since each specimen contains 30 loading cycles and each cycle includes 40 loading points and 40 unloading points, the training set contains a total of 31,200 data points, and the prediction set contains 7,200 data points.

To effectively characterize the nonlinear evolution of the hysteresis loops in the cyclic response curves, the 30 cycles within each sample are further segmented based on Fig. 4. This segmentation is implemented using the built-in enumerate function in Python to iterate through the cycles and store the data in batches. Specifically, the model input and output sequences are defined over segments consisting of five consecutive loading cycles. A sliding window approach is applied with a step size of one cycle. For example, cycles one through five constitute the first segment, cycles two through six form the second segment, and so on. Based on this method, a complete cyclic loading curve from one specimen can be divided into 26 segments. As a result, the training set is divided into a total of 338 sequence

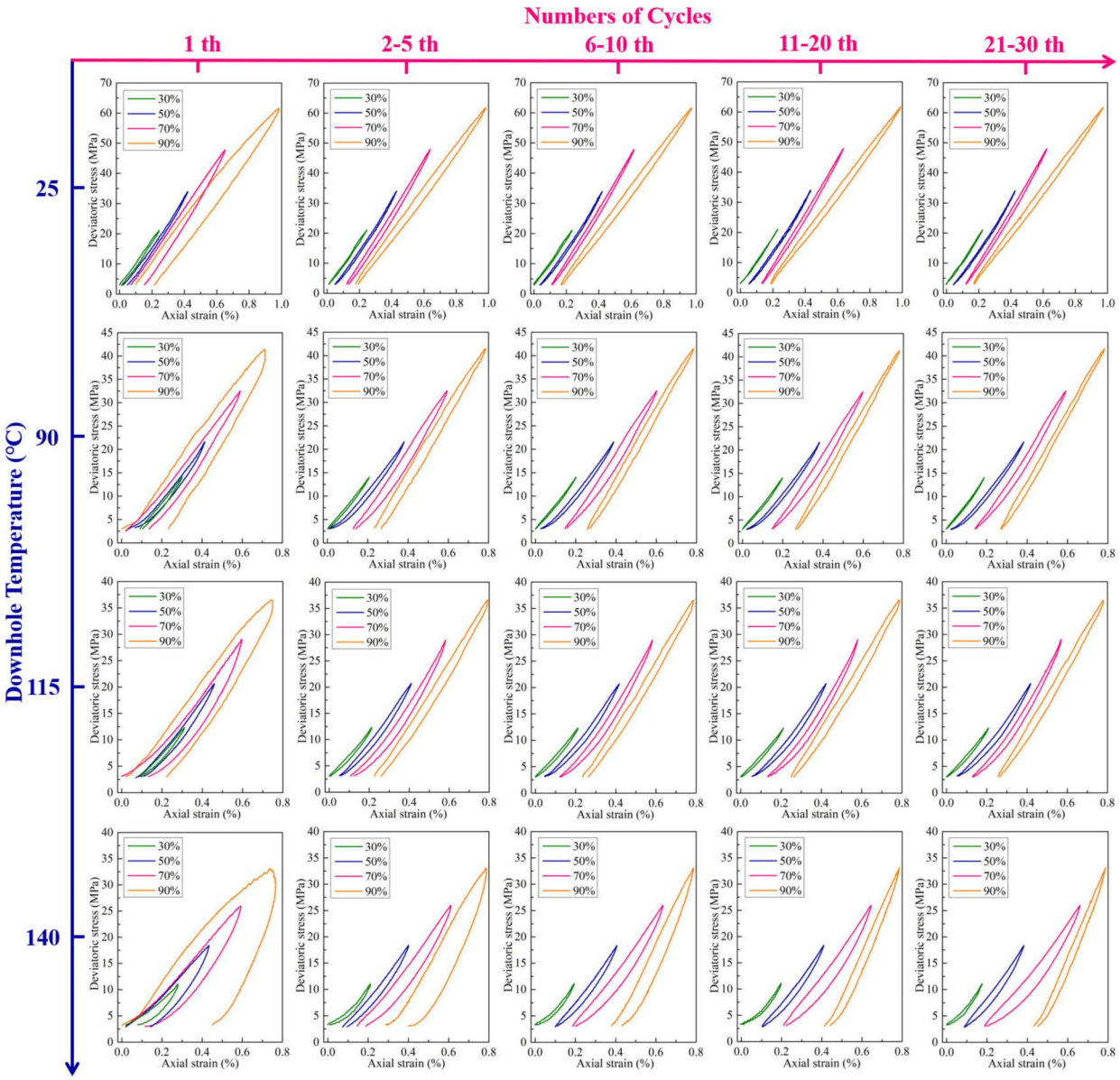


**Fig. 10** The evolution of the typical cyclic stress–strain curves (hysteresis loops) of cement samples with the number of cycles

segments, while the prediction set contains 78 segments.

The segmentation of the cyclic data by loading cycles enables the implementation of rolling prediction along the cyclic curve. However, to complete the prediction mechanism, it is also necessary to configure a single-step prediction setup for each sequence segment. Specifically, within each segment consisting of five consecutive loading cycles, the sequence data from the first four cycles are used as the model input, while the data from the fifth cycle serve as the target output for comparison during both the training and prediction stages.

### 2.3.3 Development of LSTM model

The deep learning algorithm was implemented using the open-source Python library Keras. The long short-term memory (LSTM) algorithm was selected as the foundational model to learn the long-term evolutionary and nonlinear characteristics of the cyclic hysteresis loops. This choice is based on the superior performance of LSTM in handling time-series data with historical dependencies (Zhang et al., 2021). LSTM networks are particularly effective at capturing long-range dependencies in sequential data and are equipped with gated units that can intelligently regulate the flow of information. These gates effectively mitigate the vanishing and exploding gradient problems commonly encountered in traditional recurrent neural networks (RNNs) (Chung et al., 2014; Mozaffar et al., 2019).

As defined in Section 2.3.2, four cycles of sequential data are used as the model input and one cycle of sequential data is used as the output. Therefore, the input sequence has a time step length of 320, and the output sequence has a time step length of 80. Using one loading cycle, equivalent to 80 time steps, as the sliding step for forward rolling, LSTM deep learning model is trained and evaluated on the cyclic constitutive time-series

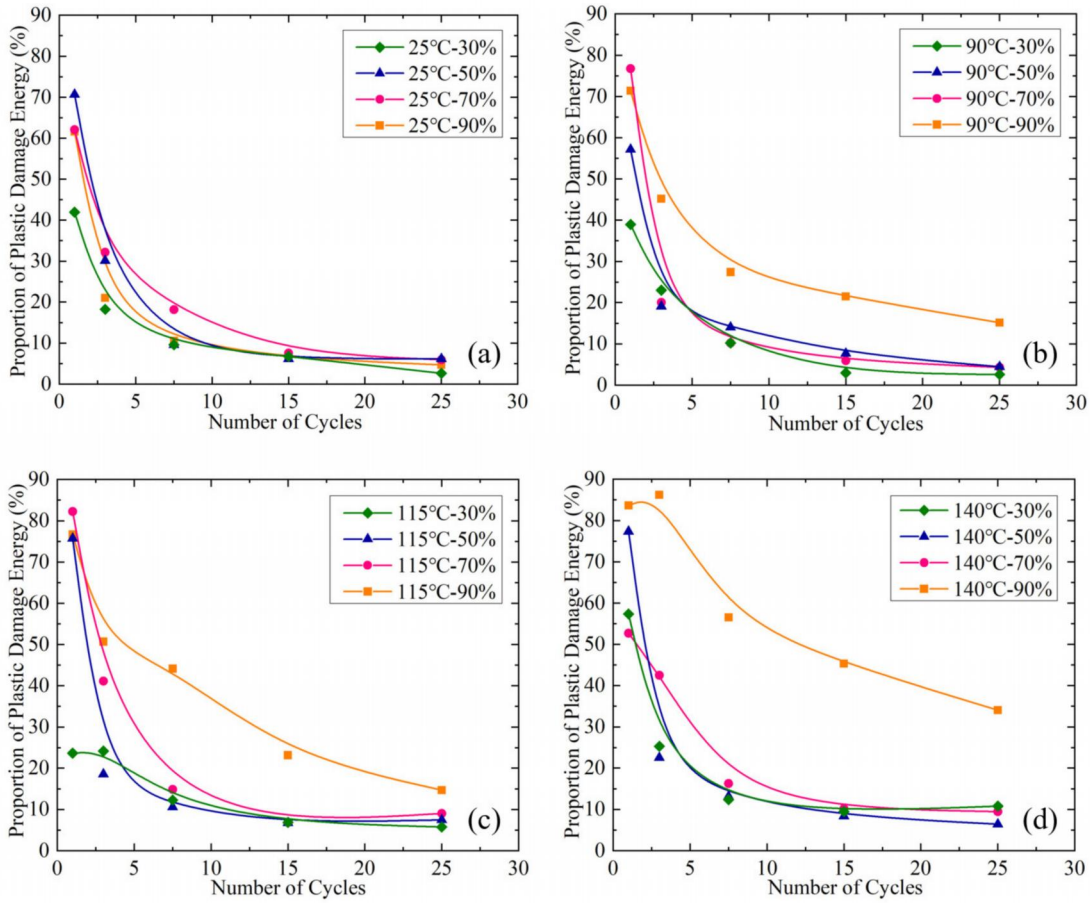


**Fig. 11** Plastic damage energy proportion of oil-well cement slurries considering different loading levels and downhole temperatures. Samples at downhole temperatures of (a)25 °C, (b)90 °C, (c)115 °C, and (d)140 °C

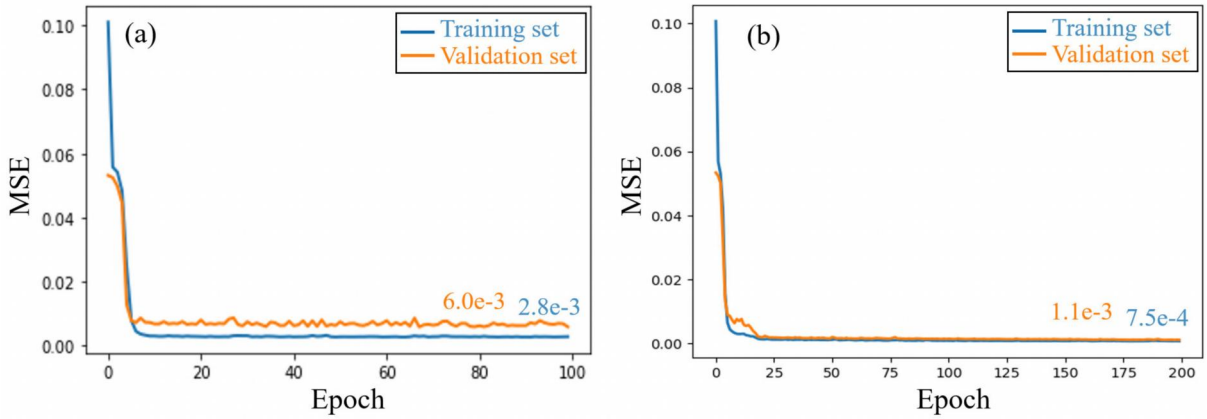


**Fig. 12** MSE error curves of training and validation sets versus training epochs across different deep learning models. (a)LSTM model, (b)PINN model

data. Model performance is assessed by comparing the predicted sequences (shown in red in Fig. 5) with the experimental results obtained from mechanical tests (shown in black in Fig. 5). Unlike traditional machine learning models, DL models start by establishing performance with a baseline model (e.g., 1–2 layers). Complexity (more layers, units) should be added incrementally only if it leads to validated improvement, thereby preventing unnecessary over-parameterization. Hyperparameters are adjusted and the models are optimized based on the accuracy of this comparison. The optimal hyperparameters of the LSTM model are summarized in Table 3, which corresponds to a network structure consisting of seven LSTM layers. Notably, because the LSTM model does not inherently support significant variation in sequence length between the input and

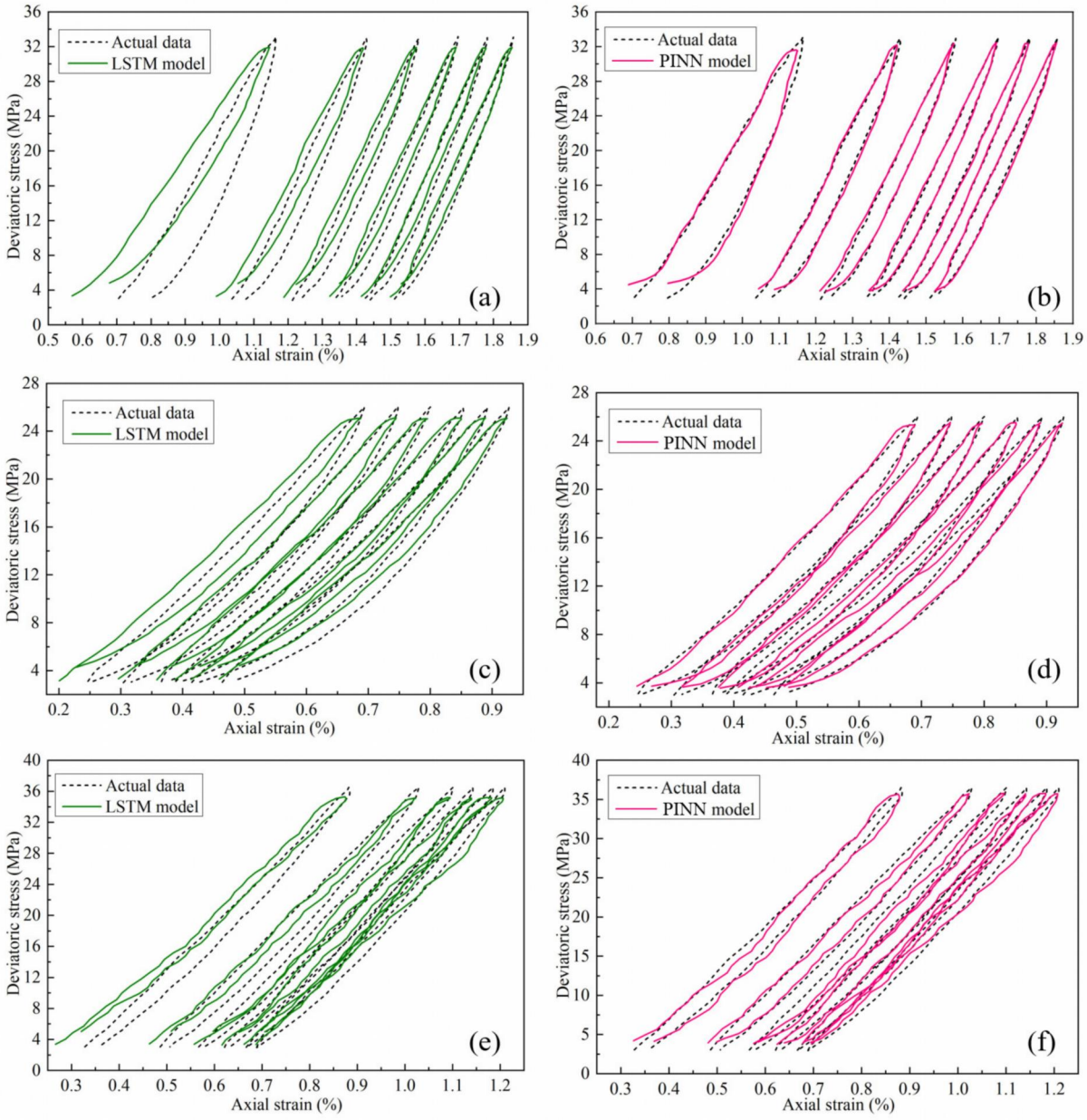


**Fig. 13** Single-step prediction performance (partial data) of the prediction set using LSTM and PINN models. (a) and (b): 140 °C downhole temperature with 90 % loading level; (c) and (d): 140 °C downhole temperature with 70 % loading level; (e) and (f): 115 °C downhole temperature with 90 % loading level

output, a RepeatVector layer is employed to bridge the encoder and decoder components. This allows the network to generate output time-series data with a different length from the input sequence.

### 2.3.4 Development of the PINN model

The physics-informed neural network (PINN), a physics-guided deep learning framework, was proposed by Raissi and co-workers (Raissi et al., 2019). Unlike traditional neural networks, this approach incorporates not only data-driven inputs but also enforces physical laws or governing equations as constraints within the training process. By embedding physical principles into the deep learning model, the PINN framework enables a unified integration of data and physics, thereby enhancing the generalization capability, applicability, and predictive performance of the model (Carleo et al., 2019; Karniadakis et al., 2021; Wang et al., 2023).

In this study, two types of physics-informed constraints are employed to integrate physical knowledge into the data-driven modeling process, aiming to promote deep interdisciplinary coupling between rock mechanics theory and artificial intelligence. The first approach involves augmenting the training dataset with synthetic data that are explicitly generated to satisfy known physical laws. This method, referred to as physics-guided learning (Xie et al., 2021; Zheng et al., 2022), enhances the model's ability to learn underlying physical mechanisms through guided supervision. The second approach introduces

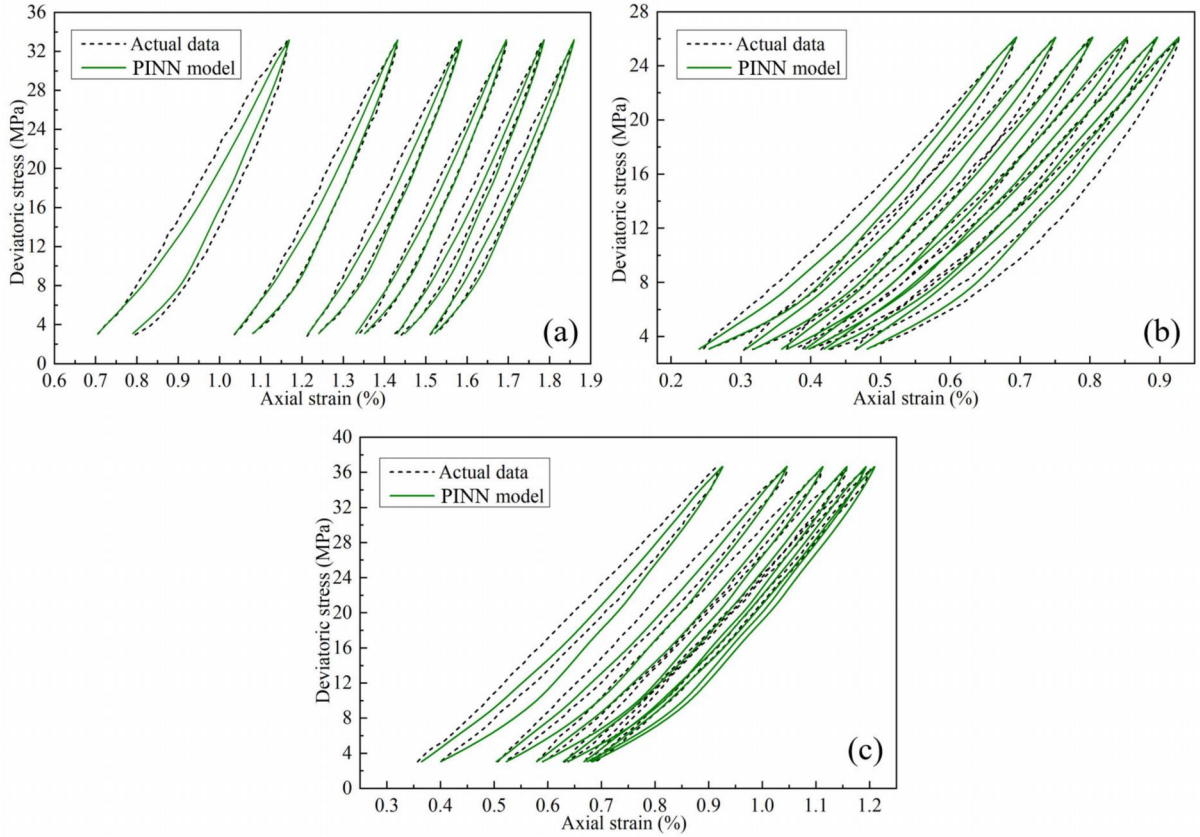


**Fig. 14** Full-cycle prediction performance (partial data) of the prediction set using PINN model. (a): 140 °C downhole temperature with 90 % loading level; (b): 140 °C downhole temperature with 70 % loading level; (c): 115 °C downhole temperature with 90 % loading level

**Tab. 3** Summary of neural network architecture and hyperparameters of LSTM model

| Layer Type | Times teps | Units/Features | Return Sequences | Output Shape | Remarks |
|---|---|---|---|---|---|
| Input Layer | 320 | 2 | — | (32, 320, 2) | — |
| LSTM | 320 | 256 | True | (32, 320, 256) | — |
| LSTM | 320 | 512 | True | (32, 320, 512) | — |
| LSTM | 320 | 256 | True | (32, 320, 256) | — |
| LSTM | — | 64 | False | (32, 64) | Last LSTM in encoder |
| RepeatVector | 80 | — | — | (32, 80, 64) | Encoder-decoder bridge |
| LSTM | 80 | 128 | True | (32, 80, 128) | First LSTM in decoder |
| LSTM | 80 | 256 | True | (32, 80, 256) | — |
| LSTM (Output) | 80 | 2 | True | (32, 80, 2) | Final prediction layer |

physical constraints or penalty terms directly into the prediction process of the deep learning model. This method, often termed process-guided or physics-constrained learning (Read et al., 2019; Xie et al., 2022), imposes additional regularization based on governing equations, which improves the model's prediction accuracy and generalization performance. Based on the two physics-informed constraint methods in single-step prediction and full-process prediction, they will combine synergistically to jointly enhance the model's prediction accuracy and effectiveness.

Specifically, in the single-step training and prediction framework, seven fatigue-related parameters with clear physical significance are manually incorporated into the dataset as part of the training input. These parameters include the accumu-

lated (residual) plastic strain $\varepsilon_i$, maximum strain $\varepsilon_i^{\max}$, total input energy $dW_i$, elastic energy $dW_i^e$, dissipated energy $dW_i^p$, damping energy $dW_i^{dd}$, and plastic damage energy $dW_i^{dp}$. The inclusion of these features is intended to enhance the model's ability to learn underlying physical mechanisms through guided supervision. To assess the effectiveness of incorporating these physics-informed features, an ablation study is conducted by comparing model performance with and without the inclusion of the new features during training. This comparison provides quantitative evidence of the value added by the physics-guided feature integration.

In addition to using the sequential data of four loading cycles (with an input time step length of 320) as input for deep learning model construction and training, an additional set of seven fatigue-related physical parameters extracted from the same four cycles (with an input time step length of 4) was also introduced as a separate input branch into an auxiliary deep learning neural network model (Fig. 6). Given the significant difference in time-step resolution between the sequential and feature data, constructing independent deep learning models for each input stream allows the respective output tensors to be closer in dimension. This setup enhances the contribution of the physical features by improving their compatibility and integration during the learning process. A Concatenate layer is used to merge the output tensors from the long-sequence and short-feature branches. Following this, a RepeatVector layer is applied to facilitate the transition between the encoder and decoder components, enabling the generation of output sequences with a time step length of 80, which differs from both input sequences. The training and prediction of the physics-constrained deep learning model are performed using a sliding window with a step size of one loading cycle. Model performance is evaluated by comparing the predicted sequences (indicated in red in Fig. 6) with experimental measurements from mechanical tests (indicated in black in Fig. 6), and the hyperparameters are tuned accordingly to optimize the model. Finally, an ablation study is conducted by comparing the physics-constrained deep learning model with a baseline hybrid deep learning model that excludes the feature input. This comparison assesses whether the inclusion of physics-informed features improves the model's capability to describe and predict the cyclic constitutive behavior of stress and strain. The optimal hyperparameters of the physics-informed deep learning model based on the LSTM architecture, which consists of ten LSTM layers, are summarized in Table 4.

### 2.3.5 Full-cycle prediction using PINN model

As shown in Fig. 7, full-cycle prediction is achieved using the physics-informed single-step prediction model through a recursive forecasting strategy. In this approach, the predicted sequence from the physics-constrained deep learning model (shown in red in Fig. 7) is recursively fed as the input for the subsequent loading cycle, thereby enabling continuous rolling prediction across the entire cyclic process. The only difference from the single-step prediction model illustrated in Fig. 6 is that, before feeding the predicted sequence into the next cycle, additional physical constraints are applied. These constraints are imposed on the endpoints of both the loading and unloading phases within each cycle to suppress the progressive accumulation and amplification of prediction errors during recursive forecasting. In addition, since the fatigue-related physical features also need to be predicted continuously, they are updated based on the output of the preceding predicted sequence. The full-cycle prediction utilizes the same network architecture and optimal hyperparameters as the physics-informed single-step prediction model. As a result, no additional training or hyperparameter tuning is required for implementing the full-cycle forecasting.

### 2.3.6 Key parameters and performance evaluation metrics

In this study, the key hyperparameters were determined manually through iterative trial-and-error, while other general hyperparameters were set to their default values. The mean squared error (MSE) was used as the loss function, and the model parameters were optimized using the Adam (Adaptive Moment Estimation) algorithm to minimize the loss. The initial learning rate was set to 0.001, and the decay rate applied after each parameter update was also set to 0.001. During the training process of the hybrid deep learning model, the training dataset was further subdivided into a training set and a validation set. The training set was used to optimize the model's trainable parameters, whereas the validation set was employed to monitor for potential overfitting or underfitting during training. Based on the validation results, the model's architecture and hyperparameters were adjusted accordingly. In this work, the validation split ratio was set to 0.23.

To quantitatively evaluate the constitutive modeling and predictive performance of different deep learning models, three commonly used evaluation metrics were adopted: the coefficient of determination ($R^2$), the mean absolute error (MAE), and the root mean square error (RMSE). In addition, the mean square error (MSE), one of the most frequently used loss functions, was employed to assess potential overfitting or underfitting during the training process.

$$R^2 = 1 - \frac{\sum_{i=1}^{n}(y_e - y_p)^2}{\sum_{i=1}^{n}(y_e - y_m)^2} \tag{8}$$

$$MAE = \frac{\sum_{i=1}^{n}|y_p - y_e|}{n} \tag{9}$$

$$RMSE = \sqrt{\frac{\sum_{i=1}^{n}(y_p - y_e)^2}{n}} \tag{10}$$

$$MSE = \frac{\sum_{i=1}^{n}(y_p - y_e)^2}{n} \tag{11}$$

In the above metrics, $y_e$ denotes the experimental (actual) data value, $y_p$ represents the predicted data value, $y_m$ is the mean of the actual data, and $n$ is the total number of data points. The coefficient of determination ($R^2$) is commonly used in regression models to evaluate the degree of agreement between predicted values and experimental measurements (Li et al.,

**Tab. 4** Summary of neural network architecture and hyperparameters of PINN model.

| Layer Type | Times teps | Units/Features | Return Sequences | Output Shape | Remarks |
|---|---|---|---|---|---|
| Sequence Input Layer | 320 | 2 | — | (32, 320, 2) | |
| LSTM Layer | 320 | 256 | True | (32, 320, 256) | |
| LSTM Layer | 320 | 512 | True | (32, 320, 512) | |
| LSTM Layer | 320 | 256 | True | (32, 320, 256) | |
| LSTM Layer | 1 | 64 | False | (32, 64) | |
| Feature Input Layer | 4 | 7 | — | (32, 4, 7) | |
| LSTM Layer | 4 | 64 | True | (32, 4, 64) | |
| LSTM Layer | 4 | 128 | True | (32, 4, 128) | |
| LSTM Layer | 1 | 16 | False | (32, 16) | |
| Concatenate Layer | 1 | 80 | — | (32, 80) | Merge sequence/feature branches |
| RepeatVector Layer | 80 | 80 | — | (32, 80, 80) | Encoder-decoder bridge |
| LSTM Layer | 80 | 128 | True | (32, 80, 128) | |
| LSTM Layer | 80 | 256 | True | (32, 80, 256) | |
| LSTM with Output Layer | 80 | 2 | True | (32, 80, 2) | Final prediction layer |

2023). An $R^2$ value closer to 1 indicates a stronger correlation and better predictive consistency. On the other hand, MAE, MSE, and RMSE are error-based metrics that quantify the deviation between predictions and actual data; lower values of these metrics indicate higher prediction accuracy and better model performance (Li et al., 2021b).

## 3 Analysis of HTHP cyclic hysteresis loops

### 3.1 Strain and dissipated energy evolutions

In the cyclic loading and unloading experiments, in order to quantitatively assess the effects of different cyclic load levels and downhole temperatures on the fatigue performance of oil-well cement paste, the accumulated plastic strain and the proportion of dissipated energy (as defined in Section 2.2) were extracted for each cycle. The corresponding results are presented in Fig. 8 and Fig. 9, respectively. The initial and linear growth stages of the reverse S-shaped relationship between accumulated plastic strain and the number of cycles are reflected (Xiao et al., 2009). Overall, with increasing cycle number, the accumulated plastic strain of samples under all temperature and loading conditions increases rapidly in the early stage, but the growth rate begins to decelerate after approximately the fifth cycle. Correspondingly, the proportion of dissipated energy is highest in the first cycle and then decreases sharply to a lower, more stable level after the fifth cycle.

At loading levels of 30 %, 50 %, and 70 % (see Figs 8(a), (b), and (c), and Figes 9(a), (b), and (c)), the residual plastic strain of the samples accumulates rapidly in the early cycles and then shows a slower rate of accumulation. After the fifth cycle, the trend becomes approximately linear. Correspondingly, the dissipated energy proportion exhibits an "L-shaped" pattern, decreasing rapidly within the first five cycles and stabilizing thereafter. As the loading level increases, the accumulated plastic strain increases significantly, and the dissipated energy proportion remains at a higher level. For example, for cement samples cured at 140 °C, increasing the loading level from 30 % to 70 % results in a 260 % increase in accumulated plastic strain by the 30th cycle, and a 110 % increase in the average dissipated energy proportion between the fifth and 30th cycles. This is because, as the loading level increases, the upper limit of the cyclic stress approaches the material's yield strength. Higher stress levels induce more microcrack accumulation and more plastic deformation within the internal pores of the cement. Therefore, a larger amount of energy is dissipated to accommodate pore deformation and microcrack growth, leading to increased accumulated plastic strain and higher dissipated energy.

When the loading level is further increased to 90 % (see Figs 8(d) and 9(d)), significant differences in fatigue performance are observed between samples cured at ambient and elevated temperatures. At 25 °C, the cement samples demonstrate stable and satisfactory fatigue resistance even under 90 % loading level. Specifically, similar to the results under 30 to 70 % loading levels, the accumulated plastic strain increases linearly after the fifth cycle, and the proportion of dissipated energy remains stable beyond this point. Compared with the 70 % loading level, the increase in accumulated plastic strain after 30 cycles at 90 % loading is only 40 %, indicating that this nanosilica cement formulation performs well under high stress at ambient

**Tab. 5** Summary of prediction performance evaluation indicators for testing sets under LSTM and PINN models.

| Model Type | Prediction Type | Performance Metrics | | |
|---|---|---|---|---|
| | | $R^2$ | MAE | RMSE |
| LSTM | Single-step prediction | 0.9178 | 0.0434 | 0.0769 |
| PINN | Single-step prediction | 0.9783 | 0.0250 | 0.0387 |
| PINN | Full-cycle prediction | 0.9656 | 0.0289 | 0.0475 |

temperature. The elastic components in the mixture contribute significantly to crack resistance and energy absorption.

In contrast, under elevated temperatures, the samples at 90 % loading level exhibit rapid nonlinear accumulation of residual plastic strain even after the fifth cycle, and the proportion of dissipated energy continues to decline in a nonlinear manner, failing to stabilize. Compared with the 70 % loading level, the increase in accumulated plastic strain at 90 % loading level is 170 % at 90 °C, 130 % at 115 °C, and 220 % at 140 °C.

These differences are strongly associated with the high-temperature curing environment. First, internal pores are regarded as initial defects prior to mechanical loading. Elevated curing temperatures lead to increased initial pore size and porosity in the cement matrix (Yang et al., 2024a), which contributes to more pronounced pore plastic deformation under the same loading level. Second, calcium silicate hydrate (C–S–H) gel is the primary phase responsible for strength in cement-based materials (Shaikh et al., 2014). However, at higher temperatures, dehydration and polymerization of C–S–H reduce the degree of interlocking between particles (Luke, 2004), which weakens cohesion and internal friction angle (Yang et al., 2024b). As a result, microcrack damage becomes more likely under cyclic loading. Both factors contribute to increased pore deformation and microcrack accumulation, which are manifested macroscopically as higher accumulated plastic strain and greater dissipated energy.

It is worth noting that due to variations in peak strength among cement samples cured at different downhole temperatures, the dissipated energy proportion in a single cycle is considered a more direct indicator of the extent of plastic deformation and damage evolution within the oil-well cement during that specific cycle. However, compared with the 70 % loading level, cement samples cured at 90 °C, 115 °C, and 140 °C exhibited significantly greater accumulation of residual plastic strain under the 90 % loading level, with increases ranging from 130 % to 220 % (as shown in Fig. 8(d)). In contrast, the average dissipated energy proportion after the fifth cycle showed only a marginal increase, ranging from 3 % to 11 % (as shown in Fig. 9(d)). This indicates that the dissipated energy proportion does not effectively capture the internal energy dissipation behavior of the cement samples under 90 % loading level. The substantial difference in hysteresis loop morphology induced by different loading levels suggests that further investigation is required, as discussed in detail in Section 3.2.

## 3.2 Evolution of the proportion of plastic damage energy

Due to measurement errors associated with the LVDT sensors used in the cyclic loading mechanical tests, fatigue-related parameters such as residual plastic strain, elastic energy, and dissipated energy exhibit certain degrees of fluctuation. To better capture the evolution of plastic damage energy with respect to the number of loading cycles, the full sequence of 30 cycles was further divided into five distinct stages based on the progression of hysteresis loop morphology: Stage I: Cycle 1, Stage II: Cycles 2 to 5, Stage III: Cycles 6 to 10, Stage IV: Cycles 11 to 20, Stage V: Cycles 21 to 30. To clearly observe the changes in hysteresis loop shape across different cycle ranges, a representative cycle was selected from each stage based on the cycle whose plastic-damage-energy proportion most closely matched the average value for that stage. The selected representative cycles and their corresponding hysteresis loops are summarized in Fig. 10.

The evolution of the average proportion of plastic damage energy for cement samples under different downhole temperatures and loading levels is summarized in Fig. 11. It can be observed that, with increasing number of cycles, the average plastic damage energy proportion decreases consistently across all samples. This trend corresponds to the gradual closure of the lower opening of the hysteresis loops (as shown in Fig. 10) and the decelerated growth of accumulated plastic strain (as shown in Fig. 8). For samples cured at ambient temperature, the cement maintained good resistance to deformation across all four loading levels (30 % to 90 %). As a result, the proportion of plastic damage energy remained lower after the fifth cycle, ranging from 2.62 % to 18.17 %. Consequently, the hysteresis loop shapes under the four loading levels are relatively similar, with small lower openings (see Fig. 10).

In contrast, for samples cured at elevated temperatures of 90 °C, 115 °C, and 140 °C, the average proportion of plastic damage energy consistently remained low beyond the 5th cycle under 30%–70% loading levels, exhibiting a gradual increase with rising temperature (2.59 %–14.02 %, 5.74 %–14.86 %, and 6.41 %–16.27 %, respectively). This indicates that cement samples at each downhole temperature exhibit similar hysteresis loop morphology (Fig. 10) and maintain a small yet stable proportion of plastic damage energy under 30 %–70 % loading conditions.

When the loading level increases to 90 %, noticeable changes in the hysteresis loop morphology are observed for cement samples at all downhole temperatures (as shown in Fig. 10). Under these conditions, the hysteresis loops tend to exhibit a nearly linear elastic stress and strain response, with minimal nonlinear hysteretic effects during unloading. This phenomenon may be attributed to further pore compaction within the cement matrix under high loading, which leads to a toughening effect in the

material. Due to the unstable and rapid increase in residual plastic strain, the lower opening of the hysteresis loop becomes significantly larger compared with those observed under 30 % to 70 % loading levels. As a result, the plastic damage energy proportion remains high throughout the 30 loading cycles and increases sharply with temperature. Specifically, the average proportion of plastic damage energy exhibiting a significant increase with rising temperature (21.36 %, 27.34 %, and 45.32 %, respectively, as shown in Fig. 11).

These findings demonstrate that the dissipated energy contained in cyclic hysteresis loops can be subdivided into plastic damage energy and damping energy. Among them, the plastic damage energy proportion provides a more accurate reflection of the morphological characteristics of the hysteresis loops under different loading levels. Moreover, this highlights that fatigue life prediction models based solely on accumulated plastic strain or total dissipated energy are insufficient to capture the complex morphological evolution of cyclic hysteresis behavior. Therefore, it is essential to further explore theoretical approaches for directly constructing cyclic stress and strain constitutive models.

## 4 Analysis of deep learning models

### 4.1 Performance evaluation of model training process

Ablation experiments were designed to implement and compare the single-step training and prediction processes of two deep learning models: the standard LSTM model and the PINN-enhanced LSTM model (i.e. PINN model). Fig. 12 presents a comparison of the training and validation errors for both hybrid models across all training epochs. The training and validation errors of both models gradually decrease as the number of training epochs increases, eventually converging to relatively small values. This indicates that two deep learning models were effectively trained without signs of overfitting or underfitting. Furthermore, a comparison of the minimum mean absolute error (MAE) values for the training and validation sets reveals that the PINN model demonstrates superior training performance. Specifically, it achieves the smallest and most consistent errors between the training and validation datasets, with a training set MAE of $7.5 \times 10^{-4}$ and a validation set MAE of $1.1 \times 10^{-3}$.

### 4.2 Performance evaluation of single-step prediction

The predictive capability of the models was evaluated using a testing set that was not included during training. The testing set consisted of three distinct loading conditions, each characterized by different hysteresis loop shapes. The single-step prediction results of the LSTM and PINN models under these conditions are illustrated in Fig. 13, and the corresponding performance metrics are summarized in Table 5. Among the models, the PINN model achieved the highest coefficient of determination ($R^2$=0.9783) and the lowest prediction errors, with a mean absolute error (MAE) of 0.0250 and a root mean square error (RMSE) of 0.0387. This model consistently demonstrated the best agreement with the actual cyclic curves across all test conditions, indicating superior single-step prediction performance and strong generalization capability. These results suggest that the incorporation of physically meaningful feature sequences significantly enhances the role of physical guidance during the deep learning process. As a result, the learning performance and prediction accuracy of PINN deep learning model architecture were substantially improved.

### 4.3 Performance evaluation of full-cycle prediction

The results presented in Fig. 13 demonstrate that the physics-constrained PINN model, enhanced with additional feature inputs, provides improved performance in single-step prediction of cyclic curves. However, the predicted residual plastic strain still deviates considerably from the experimentally measured values. It can be anticipated that, as the number of cycles increases, the overall prediction error—including that of residual plastic strain—will progressively accumulate and amplify. To address this issue, the method described in Section 2.3.5 was adopted. By incorporating additional physical constraints into the prediction process and applying a recursive prediction strategy, the same neural network architecture and hyperparameters used in the PINN single-step prediction model were directly extended to enable full-cycle prediction.

The full-cycle prediction results for all test time-series data using the physics-constrained PINN model are shown in Fig. 14, with the corresponding performance metrics summarized in Table 5. As illustrated in Fig. 14, the predicted curves align closely with the experimental cyclic curves across all test conditions, indicating excellent full-cycle prediction performance and strong generalization capability. These findings confirm that the physics-constrained PINN model achieves robust long-term prediction of the cyclic stress and strain constitutive behavior by leveraging two forms of physics-informed supervision: (1) physical guidance through the integration of fatigue-related feature data, and (2) physical constraints applied during the recursive prediction process. Furthermore, the model demonstrates high predictive accuracy, with a coefficient of determination ($R^2$) of 0.9656, and low MAE and RMSE values of 0.0289 and 0.0475, respectively, confirming its strong performance in full-cycle prediction.

## 5 Conclusions

A comprehensive analysis of 480 hysteresis loops from 16 sample groups was conducted to evaluate critical parameters including accumulated plastic strain, dissipation energy proportion, and plastic damage energy proportion. Besides, an innovative modeling methodology for cyclic constitutive prediction is developed in this study, including cycle-by-cycle data segmentation, physics-informed neural networks (PINN), and recursive prediction with physical constraints, the following key conclusions are drawn:

1. The dissipation energy within hysteresis loops can be subdivided into plastic damage energy and damping energy. The proportion of plastic damage energy more effectively characterizes hysteresis loop morphology across varying loading levels.

2. Traditional fatigue life prediction models, relying on single fatigue parameters extracted from cyclic curves, fail to capture complex evolutionary features of hysteresis loops.

3. Through normalization, down-sampling, and cycle-by-cycle segmentation of cyclic loading test data, an LSTM architecture was developed to achieve single-step rolling prediction of hysteresis loops, addressing long-term dependencies and nonlinearities.

4. By incorporating seven physically meaningful fatigue parameters into the training dataset, a PINN model achieved superior single-step prediction accuracy ($R^2$=0.9783, MAE=0.0250, RMSE=0.0387).

5. Recursive prediction augmented with physics-based constraints enabled continuous full-process rolling prediction, effectively curbing error propagation. The PINN model demonstrated sustained predictive capability for cyclic stress-strain relationships, with high $R^2$ (0.9656) and low errors (MAE=0.0289, RMSE=0.0475).

This study establishes the first application of deep learning frameworks to cyclic stress-strain constitutive modeling of oilwell cement. This innovative modeling methodology for cyclic constitutive prediction effectively overcomes the limitations of conventional mechanical models, such as mathematical complexity and poor generalizability. However, it is necessary to objectively point out that, due to the still relatively limited range of operating conditions covered by the dataset, this method remains dependent on the initial cycles of the cyclic loading tests. Further expansion of the dataset is required to enhance the model's prediction accuracy and broaden its applicability.

## Acknowledgements

This research has been funded by the National Natural Science Foundation of China (No. 52504061), the Key R & D projects of Jilin Provincial Science and Technology Department (No. 20230203121SF), the Key Lab of Geo-Exploration Instrumentation (No. GEIOF20250101), and the Engineering Research Center of Geothermal Resources Development Technology and Equipment (No. 25022), Ministry of Education, Jilin University. The authors are also sincerely grateful for the financial support from China Scholarship Council.

## Conflict of interest

The authors declare no competing interest.



## References

Banimahd M, Yasrobi SS, Woodward PK. 2005. Artificial neural network for stress–strain behavior of sandy soils: Knowledge based verification. *Computers and Geotechnics*, **32**:377–386. doi:10.1016/j.compgeo.2005.06.002.

Basheer IA. 2002. Stress-strain behavior of geomaterials in loading reversal simulated by time-delay neural networks. *Journal of Materials in Civil Engineering*, **14**:270–273. doi:10.1061/(ASCE)0899-1561(2002)14:3(270).

Basheer IA. 2000. Selection of Methodology for Neural Network Modeling of Constitutive Hystereses Behavior of Soils. *Computer-Aided Civil and Infrastructure Engineering*, **15**:445–463. doi:10.1111/0885-9507.00206.

Beaudoin JJ, Feldman RF. 1985. High-strength cement pastes - A critical appraisal. *Cement and Concrete Research*, **15**:105–116. doi:10.1016/0008-8846(85)90015-8.

Carleo G, Cirac I, Cranmer K, et al. 2019. Machine learning and the physical sciences. *Reviews of Modern Physics*, **91**:045002. doi:10.1103/RevModPhys.91.045002.

Chen BR, Feng XT, Ding WX, et al. 2004. Evolutionary neural network constitutive model for complete stress-strain relationship of rock under chemical corrosion. *Journal of Northeastern University (Science)*, **25**(7):695-698.

Chung J, Gulcehre C, Cho K, et al. 2014. Empirical evaluation of gated recurrent neural networks on sequence modeling. *arXiv preprint arXiv:1412.3555*. doi:10.48550/arXiv.1412.3555.

Deng KH, Yuan Y, Hao Y, et al. 2020. Experimental study on the integrity of casing-cement sheath in shale gas wells under pressure and temperature cycle loading. *Journal of Petroleum Science and Engineering*, **195**:107548. doi:10.1016/j.petrol.2020.107548.

Diaz MB, Kim KY, Jung SG. 2020. Effect of frequency during cyclic hydraulic fracturing and the process of fracture development in laboratory experiments. *International Journal of Rock Mechanics and Mining Sciences*, **134**:104474. doi:10.1016/j.ijrmms.2020.104474.

Eilers LH, Nelson EB, Moran LK. 1983. High-Temperature Cement Compositions - Pectolite, Scawtite, Truscottite, or Xonotlite: Which Do You Want? *Journal of Petroleum Technology*, **35**:1373–1377. doi:10.2118/9286-PA.

Ellis GW, Yao C, Zhao R, et al. 1995. Stress-strain modeling of sands using artificial neural networks. *Journal of Geotechnical Engineering*, **121**:429–435. doi:10.1061/(ASCE)0733-9410(1995)121:5(429).

Evans DJ. 2007. An appraisal of Underground Gas Storage technologies and incidents, for the development of risk assessment methodology, British Geological Survey Open Report. *British Geological Survey Open Report*.

Ghaboussi J, Sidarta DE. 1998. New nested adaptive neural networks (NANN) for constitutive modeling. *Computers and Geotechnics*, **22**:29–52. doi:10.1016/S0266-352X(97)00034-7.

Gholami R, Aadnoy B, Fakhari N. 2016. A thermo-poroelastic analytical approach to evaluate cement sheath integrity in deep vertical wells. *Journal of Petroleum Science and Engineering*, **147**:536–546. doi:10.1016/j.petrol.2016.09.024.

Gorji MB, Mozaffar M, Heidenreich JN, et al. 2020. On the potential of recurrent neural networks for modeling path dependent plasticity. *Journal of the Mechanics and Physics of Solids*, **143**:103972. doi:10.1016/j.jmps.2020.103972.

Grabowski E, Gillott JE. 1989. Effect of replacement of silica flour with silica fume on engineering properties of oilwell cements at normal and elevated temperatures and pressures. *Cement and Concrete Research*, **19**:333–344. doi:10.1016/0008-8846(89)90023-9.

Habibagahi G, Bamdad A. 2003. A neural network framework for mechanical behavior of unsaturated soils. *Canadian Geotechnical Journal*, **40**:684–693. doi:10.1139/t03-004.

Johari A, Javadi AA, Habibagahi G. 2011. Modelling the mechanical behaviour of unsaturated soils using a genetic algorithm-based neural network. *Computers and Geotechnics*, **38**:2–13. doi:10.1016/j.compgeo.2010.08.011.

Karakosta E, Lagkaditi L, ElHardalo S, et al. 2015. Pore

structure evolution and strength development of G-type elastic oil well cement. A combined 1H NMR and ultrasonic study. *Cement and Concrete Research*, **72**:90–97. doi:10.1016/j.cemconres.2015.02.018.

Karniadakis GE, Kevrekidis IG, Lu L, et al. 2021. Physics-informed machine learning. *Nature Reviews Physics*, **3**:422–440. doi:10.1038/s42254-021-00314-5.

Li K, Li D, Chen D, et al. 2021. A generalized model for effective thermal conductivity of soils considering porosity and mineral composition. *Acta Geotechnica*, **16**:3455–3466. doi:10.1007/s11440-021-01282-x.

Li KQ, Yin ZY, Zhang N, et al. 2023. A data-driven method to model stress-strain behaviour of frozen soil considering uncertainty. *Cold Regions Science and Technology*, **213**:103906. doi:10.1016/j.coldregions.2023.103906.

Li XW, Yao ZS, Huang XW, et al. 2021. Investigation of deformation and failure characteristics and energy evolution of sandstone under cyclic loading and unloading. *Rock and Soil Mechanics*, **42**:1693–1704. doi:10.16285/j.rsm.2020.1463.

Li ZY, Guo XY, Han L, et al. 2007. Improvement of latex on mechanical deformation capability of cement sheath under triaxial loading condition. *Acta Petrolei Sinica*, **28**(4):126–129. doi:10.7623/syxb200704027.

Liu XS, Ning JG, Tan YL, et al. 2016. Damage constitutive model based on energy dissipation for intact rock subjected to cyclic loading. *International Journal of Rock Mechanics and Mining Sciences*, **85**:27–32. doi:10.1016/j.ijrmms.2016.03.003.

Luke K. 2004. Phase studies of pozzolanic stabilized calcium silicate hydrates at 180 °C. *Cement and Concrete Research*, **34**:1725–1732. doi:10.1016/j.cemconres.2004.05.021.

Ma QF, Liu ZH, Qin YP, et al. 2021. Rock plastic-damage constitutive model based on energy dissipation. *Rock and Soil Mechanics*, **42**:1210–1220. doi:10.16285/j.rsm.2020.1091.

Ma QF, Qin YP, Zhou TB, et al. 2019. Mechanical properties and constitutive model of porous rock under loading and unloading. *Rock and Soil Mechanics*, **40**:2673–2685. doi:10.16285/j.rsm.2018.0513.

Mayergoyz ID. 1985. Hysteresis models from the mathematical and control theory points of view. *Journal of Applied Physics*, **57**:3803–3805. doi:10.1063/1.334925.

Meng QB, Zhang MW, Han LJ, et al. 2016. Effects of Acoustic Emission and Energy Evolution of Rock Specimens Under the Uniaxial Cyclic Loading and Unloading Compression. *Rock Mechanics and Rock Engineering*, **49**:3873–3886. doi:10.1007/s00603-016-1077-y.

Mozaffar M, Bostanabad R, Chen W, et al. 2019. Deep learning predicts path-dependent plasticity. *Proceedings of the National Academy of Sciences*, **116**:26414–26420. doi:10.1073/pnas.1911815116.

Nardin A, Schrefler B, Lefik M. 2003. Application of artificial neural network for identification of parameters of a constitutive law for soils. *Developments in Applied Artificial Intelligence*, **16**:545–554.

Pang XY, Qin JK, Sun LJ, et al. 2021. Long-term strength retrogression of silica-enriched oil well cement: A comprehensive multi-approach analysis. *Cement and Concrete Research*, **144**:106424. doi:10.1016/j.cemconres.2021.106424.

Peng XH, Wang ZC, Luo T, et al. 2008. An elasto-plastic constitutive model of moderate sandy clay based on BC-RBFNN. *Journal of Central South University of Technology*, **15**(S1):47–50. doi:10.1007/s11771-008-0312-4.

Penumadu D, Zhao R. 1999. Triaxial compression behavior of sand and gravel using artificial neural networks (ANN). *Computers and Geotechnics*, **24**(3):207–230. doi:10.1016/S0266-352X(99)00002-6.

Rafiai H, Jafari A. 2011. Artificial neural networks as a basis for new generation of rock failure criteria. *International Journal of Rock Mechanics and Mining Sciences*, **48**(7):1153–1159. doi:10.1016/j.ijrmms.2011.06.001.

Raissi M, Perdikaris P, Karniadakis GE. 2019. Physics-informed neural networks: A deep learning framework for solving forward and inverse problems involving nonlinear partial differential equations. *Journal of Computational Physics*, **378**:686–707. doi:10.1016/j.jcp.2018.10.045.

Rashidian V, Hassanlourad M. 2014. Application of an Artificial Neural Network for Modeling the Mechanical Behavior of Carbonate Soils. *International Journal of Geomechanics*, **14**(1):142–150. doi:10.1061/(ASCE)GM.1943-5622.0000299.

Read JS, Jia X, Willard J, et al. 2019. Process-guided deep learning predictions of lake water temperature. *Water Resources Research*, **55**:9173–9190. doi:10.1029/2019WR024922.

Romo MP, García SR, Mendoza MJ, et al. 2001. Recurrent and Constructive-Algorithm Networks For Sand Behavior Modeling. *International Journal of Geomechanics*, **1**(4):371–387. doi:10.1080/15323640108500167.

Shadravan A, Kias E, Lew R, et al. 2015. Utilizing the Evolving Cement Mechanical Properties under Fatigue to Predict Cement Sheath Integrity. *SPE Kuwait Oil & Gas Show and Conference*. doi:10.2118/175231-MS.

Shaikh FUA, Supit SWM, Sarker PK. 2014. A study on the effect of nano silica on compressive strength of high volume fly ash mortars and concretes. *Materials & Design*, **60**:433–442. doi:10.1016/j.matdes.2014.04.025.

Shi LL, Zhang J, Zhu QZ, et al. 2022. Prediction of mechanical behavior of rocks with strong strain-softening effects by a deep-learning approach. *Computers and Geotechnics*, **152**:105040. doi:10.1016/j.compgeo.2022.105040.

Song ZY, Frühwirt T, Konietzky H. 2018. Characteristics of dissipated energy of concrete subjected to cyclic loading. *Construction and Building Materials*, **168**:47–60. doi:10.1016/j.conbuildmat.2018.02.076.

Tan YL, Wang CQ. 2001. A fast approaching model for rock constitutive equation by radial basis function neural network. *Chinese Journal of Geotechnical Engineering*, **23**(1):14–17.

Qiu TM, Yuntian F, Mengqi W, et al. 2021. Constitutive relations of granular materials by integrating micromechanical knowledge with deep learning. *Chinese Journal of Theoretical and Applied Mechanics*, **53**(9):2404–2415. doi:10.6052/0459-1879-21-221.

Wang MQ, Qu TM, Guan SH, et al. 2022. Data-driven strain–stress modelling of granular materials via temporal convolution neural network. *Computers and Geotechnics*, **152**:105049. doi:10.1016/j.compgeo.2022.105049.

Wang Y, Wang WK, Ma ZT, et al. 2023. A deep learning approach based on physical constraints for predicting soil moisture in unsaturated zones. *Water Resources Research*, **59**(11):e2023WR035194. doi:10.1029/2023WR035194.

Wu L, Ma D, Wang Z, et al. 2023. A deep CNN-based constitutive model for describing of statics characteristics of rock materials. *Engineering Fracture Mechanics*, **279**:109054. doi:10.1016/j.engfracmech.2023.109054.

Wu ZH, Song ZY, Tan J, et al. 2020. The evolution law of rock energy under different graded cyclic loading and unloading modes. *Journal of Mining Safety Engineering*, **37**:836–845. doi:10.13545/j.cnki.jmse.2020.04.23.

Xi Y, Li J, Tao Q, et al. 2020. Experimental and numerical investigations of accumulated plastic deformation in cement sheath during multistage fracturing in shale gas wells.

*Journal of Petroleum Science and Engineering*, **187**:106790. doi:10.1016/j.petrol.2019.106790.

Xiao JQ, Ding DX, Jiang FL, et al. 2010. Fatigue damage variable and evolution of rock subjected to cyclic loading. *International Journal of Rock Mechanics and Mining Sciences*, **47**(3):461–468. doi:10.1016/j.ijrmms.2009.11.003.

Xiao JQ, Ding DX, Xu G, et al. 2009. Inverted S-shaped model for nonlinear fatigue damage of rock. *International Journal of Rock Mechanics and Mining Sciences*, **46**(3):643–648. doi:10.1016/j.ijrmms.2008.11.002.

Xie K, Liu P, Zhang J, et al. 2021. Physics-guided deep learning for rainfall-runoff modeling by considering extreme events and monotonic relationships. *Journal of Hydrology*, **603**:127043. doi:10.1016/j.jhydrol.2021.127043.

Xie W, Kimura M, Takaki K, et al. 2022. Interpretable framework of physics-guided neural network with attention mechanism: simulating paddy field water temperature variations. *Water Resources Research*, **58**:e2021WR030493. doi:10.1029/2021WR030493.

Xiong W, Wang J, Wu M. 2023. Data-driven constitutive modelling of granular soils considering multiscale particle morphology. *Computers and Geotechnics*, **162**:105699. doi:10.1016/j.compgeo.2023.105699.

Yang C, Kim Y, Ryu S, et al. 2020. Prediction of composite microstructure stress-strain curves using convolutional neural networks. *Materials & Design*, **189**:108509. doi:10.1016/j.matdes.2020.108509.

Yang HZ, Wang L, Yang CH, et al. 2024. Mechanical performance of oil-well cement slurries cured and tested under high-temperatures and high-pressures for deep-well applications. *Cement and Concrete Research*, **175**:107355. doi:10.1016/j.cemconres.2023.107355.

Yang HZ, Wang L, Huang GP, et al. 2024. Effects of compressive cyclic loading on the fatigue properties of oil-well cement slurries serving in deep downhole environments. *Construction and Building Materials*, **428**:136360. doi:10.1016/j.conbuildmat.2024.136360.

Yin HW, Ma HL, Shi XL, et al. 2024. Leakage Risk Analysis of Underground Gas Storage Salt Caverns with Microleakage Interlayer in Bedded Rock Salt of Jiangsu, China. *Rock Mechanics and Rock Engineering*, **58**:2829–2845. doi:10.1007/s00603-024-04316-4.

Youssef MAH, Camilo M, Jamshid G, et al. 2006. Novel Approach to Integration of Numerical Modeling and Field Observations for Deep Excavations. *Journal of Geotechnical and Geoenvironmental Engineering*, **132**(8):1019–1031. doi:10.1061/(ASCE)1090-0241(2006)132:8(1019).

Zhang P, Yin Z, Jin Y. 2021. State-of-the-art review of machine learning applications in constitutive modeling of soils. *Archives of Computational Methods in Engineering*, **28**:3661–3686. doi:10.1007/s11831-020-09524-z.

Zheng Y, Liu P, Cheng L, et al. 2022. Extracting operation behaviors of cascade reservoirs using physics-guided long-short term memory networks. *Journal of Hydrology: Regional Studies*, **40**:101034. doi:10.1016/j.ejrh.2022.101034.

Zhu JH, Zaman MM, Anderson SA. 1998. Modelling of shearing behaviour of a residual soil with Recurrent Neural Network. *International Journal for Numerical and Analytical Methods in Geomechanics*, **22**:671–687. doi:10.1002/(SICI)1096-9853(199808)22:8<671::AID-NAG939>3.0.CO;2-Y.